buildings

MDPI

Article

Ground Settlement Susceptibility Assessment in Urban Areas Using PSInSAR and Ensemble Learning: An Integrated Geospatial Approach

WoonSeong Jeong [1], Moon-Soo Song [2,*,†], Sang-Guk Yum [2,*,†] and Manik Das Adhikari [2,*,†]

[1] Department of Architectural Engineering, Chungbuk National University, Cheongju 28644, Republic of Korea; wsjeong@cbnu.ac.kr
[2] Department of Civil and Environmental Engineering, Gangneung-Wonju National University, Gangneung 25457, Republic of Korea
* Correspondence: songms0722@gwnu.ac.kr (M.-S.S.); skyeom0401@gwnu.ac.kr (S.-G.Y.); manik@gwnu.ac.kr (M.D.A.)
† These authors contributed equally to this work.

Abstract

Ground settlement is a multifaceted geological phenomenon driven by natural and man-made forces, posing a significant impediment to sustainable urban development. Thus, ground settlement susceptibility (GSS) mapping has emerged as a critical tool for understanding and mitigating cascading hazards in seismically active and anthropogenically modified sedimentary basins. Here, we develop an integrated framework for assessing GSS in the Pohang region, South Korea, by integrating Persistent Scatterer Interferometric Synthetic Aperture Radar (PSInSAR)-derived vertical land motion (VLM) data with seismological, geotechnical, and topographic parameters (i.e., peak ground acceleration (PGA), effective shear-wave velocity ($V_s{}^{30}$), site period (T_s), general amplification factor (A_F), seismic vulnerability index (K_g), soil depth, topographic slope, and landform classes) through ensemble machine learning models such as Random Forest (RF), XGBoost, and Decision Tree (DT). Analysis of 56 Sentinel-1 SLC images (2017–2023) revealed persistent subsidence concentrated in Quaternary alluvium, reclaimed coastal plains, and basin-fill deposits. Among the tested models, RF achieved the best performance and strongly agreed with field evidence of sand boils, liquefaction, and structural damage from the 2017 Pohang earthquake. The very-high-susceptibility zones exhibited mean subsidence rates of −3.21 mm/year, primarily within soft sediments ($V_s{}^{30}$ < 360 m/s) and areas of thick alluvium deposits. Integration of the optimal RF-based GSS index with regional building inventories revealed that nearly 65% of existing buildings fell within high- to very-high-susceptibility zones. The proposed framework demonstrates that integrating PSInSAR and ensemble learning provides a robust and transferable approach for quantifying ground settlement hazards and supporting risk-informed urban planning in seismically active and complex geological coastal environments.

Keywords: PSInSAR; ground settlement susceptibility; ensemble learning; urban vulnerability; resilience planning

check for updates

Academic Editors: Dong Li, Zhenhao Zhang and Yue-Ling Long

Received: 4 November 2025
Revised: 25 November 2025
Accepted: 26 November 2025
Published: 2 December 2025

Citation: Jeong, W.; Song, M.-S.; Yum, S.-G.; Adhikari, M.D. Ground Settlement Susceptibility Assessment in Urban Areas Using PSInSAR and Ensemble Learning: An Integrated Geospatial Approach. *Buildings* **2025**, *15*, 4364. https://doi.org/10.3390/buildings15234364

Copyright: © 2025 by the authors. Licensee MDPI, Basel, Switzerland. This article is an open access article distributed under the terms and conditions of the Creative Commons Attribution (CC BY) license (https://creativecommons.org/licenses/by/4.0/).

1. Introduction

1.1. Background of the Study

Ground settlement represents a significant geohazard that poses a threat to the safety, serviceability, and resilience of urban infrastructure worldwide. These cascading hazards

may arise from natural processes and anthropogenic activities, with seismic excitations as a significant trigger for sudden and differential ground deformation. During a seismic event, the loss of contact between soil particles causes the ground to behave like a fluid, resulting in massive deformation and the potential for structural collapse [1]. Beyond earthquakes, other mechanisms include consolidation settlement, a time-dependent process in which water is expelled from saturated, fine-grained soils under sustained load, and creep settlement, a slow, continuous deformation observed in highly compressible soils [2]. Therefore, the extent and severity of ground settlement are strongly influenced by subsurface properties, including geotechnical, geological, topographical, and seismological conditions. The global proliferation of sinking cities highlights that land subsidence is not a localized issue but a widespread geohazard affecting rapidly urbanizing regions worldwide [3–5]. Several megacities have experienced chronic settlement linked to soft soil consolidation and anthropogenic drivers, such as Mexico City subsiding by up to 30 cm/year due to lacustrine deposit consolidation [6], Jakarta experiencing severe land subsidence aggravated by groundwater overextraction [3], and Shanghai facing settlement related to reclamation and soft clay compaction [7]. While such examples highlight the long-term geotechnical challenges of urban development, earthquake-induced settlement has also produced catastrophic urban impacts. For example, the 1964 Niigata earthquake in Japan caused widespread liquefaction and building tilting due to ground settlement [8], the 1994 Northridge earthquake in Simi Valley, California, demonstrated significant differential settlements due to both liquefaction and dry shaking [9], the 1999 İzmit earthquake in Turkey triggered localized subsidence and infrastructure damage on alluvial plains [10], the 2001 Bhuj earthquake in India led to various ground deformations, including fissures, lateral spreads, and subsidence, primarily due to liquefaction in the Kachchh region [11], the 2011 Christchurch earthquake in New Zealand significantly impacted ground settlement in the region, particularly due to liquefaction and lateral spreading [12], and, similarly, the 2011 Tōhoku earthquake in Japan produced severe coastal settlement and lateral spreading in reclaimed port areas [13]. This compounding effect highlights that a city's susceptibility to ground settlement is an aggregate risk, where pre-existing subsidence conditions may be catastrophically triggered or amplified by a seismic excitation.

In South Korea, ground settlement hazards have received increasing attention following the 2017 Pohang earthquake of moment magnitude M5.4, which caused significant ground damage, building collapse, liquefaction, and settlement in residential and industrial areas [14–18]. The earthquake originated from a shallow rupture, producing measurable surface displacements and inducing significant ground settlement that damaged buildings, roads, and lifeline infrastructure, particularly in areas with soft Quaternary alluvium [19,20]. Post-event investigations highlighted that reclaimed and unconsolidated deposits in Pohang were highly vulnerable to differential settlement, compaction, and ground motion amplification [14,16]. Kim et al. [21] documented different damage grades for a specific building based on an extensive field survey conducted after the Pohang earthquake and observed that the ground conditions influenced the building damage. Similarly, Gihm et al. [15] documented extensive sand blows and lateral spread over the Quaternary sediment cover in the Pohang region. Kim et al. [22] further demonstrated that sand boils near the epicenter closely matched the calculated high liquefaction potential index (LPI) zones, with boil area increasing with LPI, indicating that subsurface liquefaction was the main driver of observed ground settlement. The spatial distribution of these ground failures strongly reflected the underlying geological framework, including basin geometry, stratigraphic architecture, and fault systems [23]. Since the Pohang earthquake, understanding settlement mechanisms and mapping settlement-susceptible zones due to seismic excitation have become crucial for safeguarding urban infrastructure and reducing cascading disaster

risks in the region. In addition, several studies have reported substantial ground subsidence in reclaimed coastal cities across South Korea, including Mokpo [2], Busan [24,25], and Incheon [26,27]. Furthermore, numerous studies have documented over 1127 subsidence incidents in major metropolitan areas during the past decade, primarily driven by intense precipitation, deteriorating underground infrastructure, groundwater fluctuations, and inadequate post-construction compaction [2,28–30]. Therefore, given South Korea's extensive reliance on coastal reclamation for urban expansion and its recent seismic exposure, continuous monitoring of ground settlement dynamics is essential to ensure the safety of critical infrastructure and long-term serviceability.

The present study aims to address this gap by integrating advanced remote sensing and machine learning techniques for GSS mapping. In the present study, we utilized the PSInSAR technique to quantify long-term VLM and combine it with ensemble learning methods to predict GSS based on geotechnical, seismological, and topographic attributes. By linking PSInSAR-derived VLM with machine learning-based predictive models, this study provides a robust tool for urban planners, engineers, and policymakers to enhance the resilience of urban infrastructure.

1.2. Literature Review

GSS mapping is the process of identifying areas prone to settlement based on various predisposing factors. Accordingly, identifying zones susceptible to settlement is essential for proactive planning, sustainable development, and disaster risk reduction. Traditional methods for creating GSS maps often relied on geodetic survey, geotechnical testing, and geological data. While these approaches provide highly accurate point-scale measurements, their spatial and temporal coverage limits their utility for regional-scale susceptibility mapping. Subsequently, since the emergence of radar interferometry, i.e., the PSInSAR technique, it has often been used to monitor ongoing ground movement in urban and industrial environments with unprecedented precision [2,31]. Additionally, recent advancements have shifted the focus toward data-driven, statistical, and machine learning-based approaches that can integrate various influencing factors to produce high-resolution, reliable geohazard-susceptible maps.

Numerous studies have utilized PSInSAR and multi-temporal SAR data to monitor rapid subsidence in coastal cities such as Jakarta, Shenzhen, New Orleans, and Ho Chi Minh, emphasizing infrastructure vulnerabilities and the urgent need for mitigation [3–5,32–34]. For example, Chaussard et al. [3] reported subsidence rates exceeding 200 mm/year in Jakarta using ALOS SAR time series. Tay et al. [5] combined Sentinel-1 SAR and GNSS data to quantify VLM in 48 major coastal cities, revealing pronounced sinking across Southeast Asia. PSInSAR analysis by Aziz Zanjani et al. [35] identified localized settlement in Miami's barrier islands driven by construction and interbedded sand layers. Similarly, several researchers used InSAR to monitor earthquake-induced displacement. For example, Sun et al. [36] utilized InSAR and PolSAR to evaluate ground displacement and building damage resulting from the 2021 Baicheng earthquake in China. Suresh and Yarrakula [37] utilized Sentinel-1 data and the DInSAR technique to monitor the surface deformation of the 2017 M_w 7.3 earthquake that occurred in Iran/Iraq and found a maximum deformation of 85.1 cm.

In South Korea, Sengupta et al. [27] reported subsidence exceeding 20 cm/year in reclaimed coastal areas of Incheon using Sentinel-1A SLC data. Jeong et al. [2] applied Sentinel-1 SLC SAR datasets and detected continuous subsidence in Mokpo due to soft-soil compaction. In Busan, Nur et al. [24] documented subsidence up to 20.98 mm/year at the Noksan National Industrial Complex on deep soft ground using Sentinel-1 and the PSInSAR technique. Similarly, Park and Hong [25] applied SBAS to Sentinel-1 and ALOS

PALSAR, identifying a maximum settlement of −4.3 cm/year in southwestern Busan due to compaction of reclaimed soil. Yun et al. [38] reported ongoing deformation along a fault in Ulsan up to 15 mm/year using Sentinel-1 and PSInSAR. Earthquake-induced displacements were quantified by Choi et al. [20] using DInSAR on pre- and post-Sentinel-1 data for the Pohang earthquake, revealing ground shifts corresponding to the rupture plane. Furthermore, Palanisamy Vadivel et al. [39] reported a VLM of −2.55 cm/year at the Pohang Tide Gauge Station, based on Sentinel-1 time series data and the PSInSAR technique, and validated by nearby GPS data. Moreover, Ramirez et al. [40] further demonstrated the utility of InSAR in addressing geotechnical issues across multiple sites in Korea. The above review highlights that InSAR and time-series SAR effectively quantify ground deformation from both natural and anthropogenic sources, and are essential for assessing seismic hazards, geological vulnerabilities, and the impacts of urban development, as well as supporting sustainable infrastructure planning.

On the other hand, to model geohazard susceptibility, numerous researchers have integrated InSAR-derived deformation with other influencing factors using statistical and machine learning algorithms (e.g., [41–50]). For example, Fadhillah et al. [43] used PSInSAR-derived displacement data with ten potential subsidence-related factors (elevation, slope, aspect, curvature, distance to fault, Twi, distance to river, water bodies, land use, and lithology) and three ensemble models (LogitBoost, Bagging, and Multiclass Classifier) to map land subsidence susceptibility in Seoul, evaluating infrastructure stability relative to subsurface geology. Similarly, Yaragunda et al. [48] integrated SBAS-InSAR data with Random Forest and XGBoost models to develop ML-based subsidence susceptibility maps, while Chen et al. [42] and Hussain et al. [44] applied hybrid ML approaches for comprehensive subsidence susceptibility and risk assessment in seismically active and rapidly urbanizing regions. Likewise, applications of ensemble learning for landslides, subsidence, and liquefaction have consistently demonstrated improved predictive accuracy and robustness [18,51–54]. However, despite these advances, limited efforts have combined PSInSAR-derived deformation data with ensemble ML algorithms for comprehensive GSS assessment in South Korea, particularly in seismicity-prone and industrial coastal cities. On the other hand, selecting appropriate geotechnical and seismological factors is critical for identifying high-risk areas, as multiple direct and indirect elements influence subsidence [14,18,44]. Therefore, identifying the primary factors contributing to subsidence is essential for spatial modeling of ground settlement. Subsequently, this study assesses GSS in the Pohang region to evaluate its potential damage to urban infrastructure by integrating PSInSAR-derived VLM with multiple influencing factors of ground settlement using an ensemble of machine learning algorithms. The ongoing ground deformation was derived from 56 Sentinel-1 SLC datasets (2017–2023) using the PSInSAR technique. Thereafter, seismological and geotechnical influencing factors (i.e., PGA, seismic site class ($V_s{}^{30}$), site period (T_s), general amplification factor (A_F), and seismic vulnerability index (K_g)) were calculated based on in-situ reported data and established empirical relations. Additional influencing factors, including soil depth, topographic landforms, and slope, were extracted from high-resolution LiDAR DEM and digital soil data. Finally, we developed an ML-based predictive model to map GSS by quantifying the relationship between the PSInSAR-derived VLM and the influencing factors. The resulting GSS map was validated against field-reported damage and liquefaction/sand boil sites to ensure its reliability for practical urban infrastructure management.

2. Study Area

The Korean Peninsula is situated within a stable continental region, far from active plate boundaries; it is seismically influenced by intraplate stress transfer, far-field effects of

subduction, and reactivation of pre-existing faults [55,56]. Historically, seismicity across the peninsula has been considered moderate, with most recorded events having magnitudes below M_w 6.0 (Figure 1a). Seismotectonically, the peninsula is characterized by numerous NNE–SSW to NE–SW trending faults, many of which are related to Mesozoic tectonic events. Seismic hazard assessments consistently highlight the southeastern Korean Peninsula as one of the most seismically active zones, with higher peak ground acceleration levels than the western regions [55,57]. Although seismic design codes have been progressively revised, much of Korea's urban infrastructure remains vulnerable to ground shaking, settlement, and liquefaction, including older residential buildings, industrial facilities, and reclaimed coastal developments.

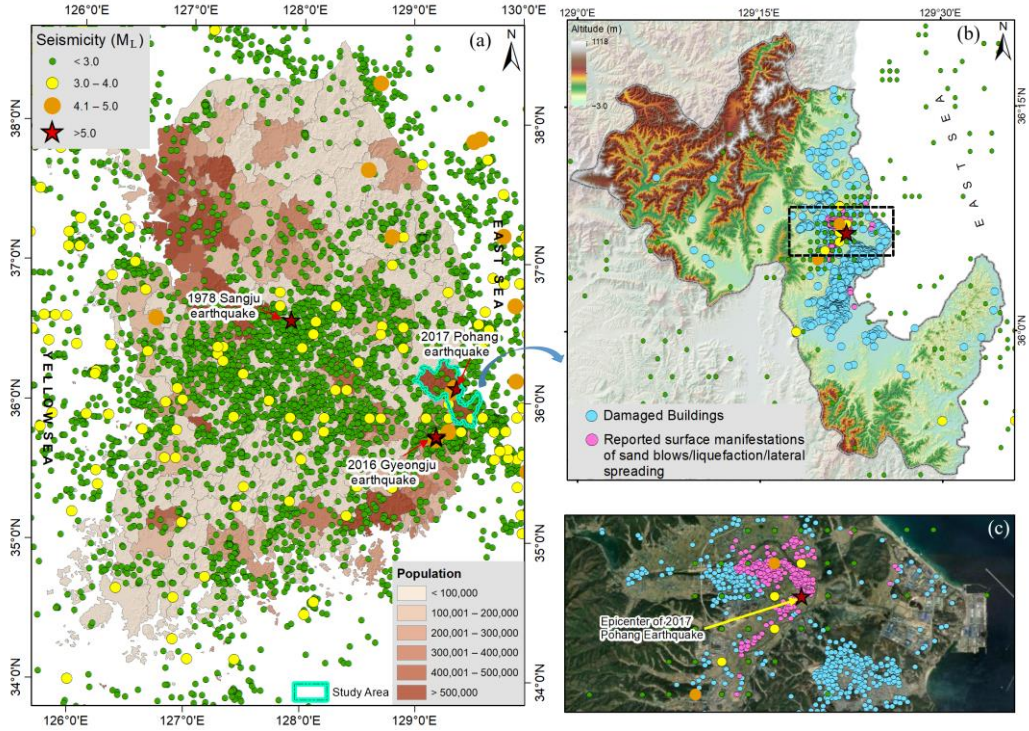

Figure 1. Study area map exhibits (**a**) seismicity distribution of South Korea from 1978 to 2022 (https://necis.kma.go.kr/, accessed on 20 August 2025), and (**b**,**c**) the distribution of damaged buildings and surface manifestations of sand blows/liquefaction/lateral spreading due to the Pohang earthquake adapted and complied from [15,21,23,58] (Note: the compilation of multiple field evidence datasets from [15,21,23,58] may include positional uncertainties related to georeferencing and digitization).

Geologically, the Pohang Basin in southeastern Korea is a Cenozoic sedimentary basin comprising unconsolidated to semi-consolidated sandstone, shale, conglomerate, and volcaniclastic deposits overlying Mesozoic granitic and metamorphic basement rocks [16,59]. Formed during the middle Miocene (~20 Ma), it contains 200–400 m of non-marine to deep-marine sediments capped by less than 1 m of Quaternary alluvium [14,16]. These loose, fine-grained deposits exhibit high susceptibility to seismic amplification and post-seismic settlement. The basin is segmented by normal and transfer faults, forming several sub-basins, including the Heunghae sub-basin, which is the epicentral area of the 2017 Pohang earthquake [60]. The Yangsan–Ulsan Fault system accommodates ongoing Cenozoic deformation, with Quaternary faulting reflecting ENE–WSW compression [19,61]. Recurrent tectonic subsidence and sedimentation have produced thick, compressible strata prone to consolidation and liquefaction under dynamic loading [23]. It was observed that low-lying urban and industrial zones are primarily underlain by Quaternary alluvium and reclaimed coastal deposits, where high groundwater levels and low shear strength heighten the risk of liquefaction [15,22]. Geomorphologically, the basin comprises coastal

plains, alluvial terraces, and gently sloping hills shaped by the Hyeongsan River system. The extensive reclamation of tidal flats for industrial and residential use has further altered subsurface conditions, thereby increasing susceptibility to settlement and liquefaction.

The 2017 Pohang earthquake, which struck Heunghae-eup in Buk-gu, Pohang City, southeastern Korea, remains one of the most significant seismic disasters in modern Korean history due to its induced origin and substantial socioeconomic impacts. Despite its moderate magnitude, the event triggered extensive ground deformation, highlighting the high vulnerability of reclaimed and alluvial deposits to seismic loading. Widespread soil liquefaction and settlement, rarely observed at such a scale in South Korea, fundamentally reshaped national perceptions of seismic hazard [19,52]. Comprehensive field investigations (i.e., [15–17,20,21,23]) have documented severe infrastructure damage concentrated in areas with soft ground. The earthquake affected more than 2500 houses, 227 schools, 11 bridges, and numerous roads, resulting in an estimated economic loss of approximately USD 52 million [16]. Kim et al. [21] classified 2650 surveyed buildings based on structural assessments into the following three categories: 2340 with minor (Grade 1), 177 with moderate (Grade 2), and 133 with severe (Grade 3) damage. Field mapping revealed over 600 features, including sand boils, fissures, and lateral spreading, across reclaimed zones and riverbanks [15,23,58], with liquefaction craters exceeding 2 m in diameter [16]. The spatial distribution of reported damaged buildings and surface manifestations of sand blows/liquefaction/lateral spreading due to the Pohang earthquake is depicted in Figure 1b,c. InSAR analysis further detected coseismic deformation ranging from 5 cm to −5 cm across central Pohang [62]. Moreover, subsurface investigations have identified liquefiable strata at depths ranging from 1.5 to 15 m [18,22,52]. The resulting failures included building tilting, retaining wall collapse, and road settlement [15,21]. Consequently, the 2017 event confirmed that even moderate-magnitude earthquakes can trigger severe liquefaction and settlement [18]. Kim et al. [22] also noted that, compared with the 2016 Gyeongju earthquake (M 5.5), greater damage in Pohang is attributed to basin amplification and thick alluvial infill. Thus, the geological and geomorphic factors of the Pohang region highlight the need for a comprehensive GSS assessment to support seismic resilience and sustainable urban management.

3. Data and Methodology

Ground settlement is a complex geomechanical process resulting from both natural and anthropogenic influences, posing a significant constraint on the development of sustainable urban infrastructure. The 2017 Pohang earthquake demonstrated that even moderate-magnitude events can induce severe settlement under unfavorable site conditions, particularly where shallow hypocenters, unconsolidated sediments, and anthropogenic activities coincide. This highlights the necessity for continuous deformation monitoring and predictive mapping of settlement susceptibility. Accordingly, GSS in the Pohang region was evaluated by integrating PSInSAR-derived VLM with key geotechnical, seismological, and topographical predictors through an ensemble machine learning framework. The major objectives of the present investigation are (a) evolution of ongoing VLM based on the time series sentinel-1 SLC using the advanced PSInSAR technique, (b) analysis of site characterization factors (i.e., $V_s{}^{30}$, site periods, general site amplification, and seismic vulnerability index) and seismological factor (i.e., PGA), (c) development of an ensemble of ML-based predictive models to map GSS by quantifying the relationship between the PSInSAR-derived VLM and the influencing factors, (d) evaluation of building damage potential based on the predicted optimized ML model, and (e) model validation based on the independent reported building damage and liquefaction/sand boils/lateral spreading

evidence. The proposed integrated geospatial–ML framework for GSS modeling is depicted in Figure 2.

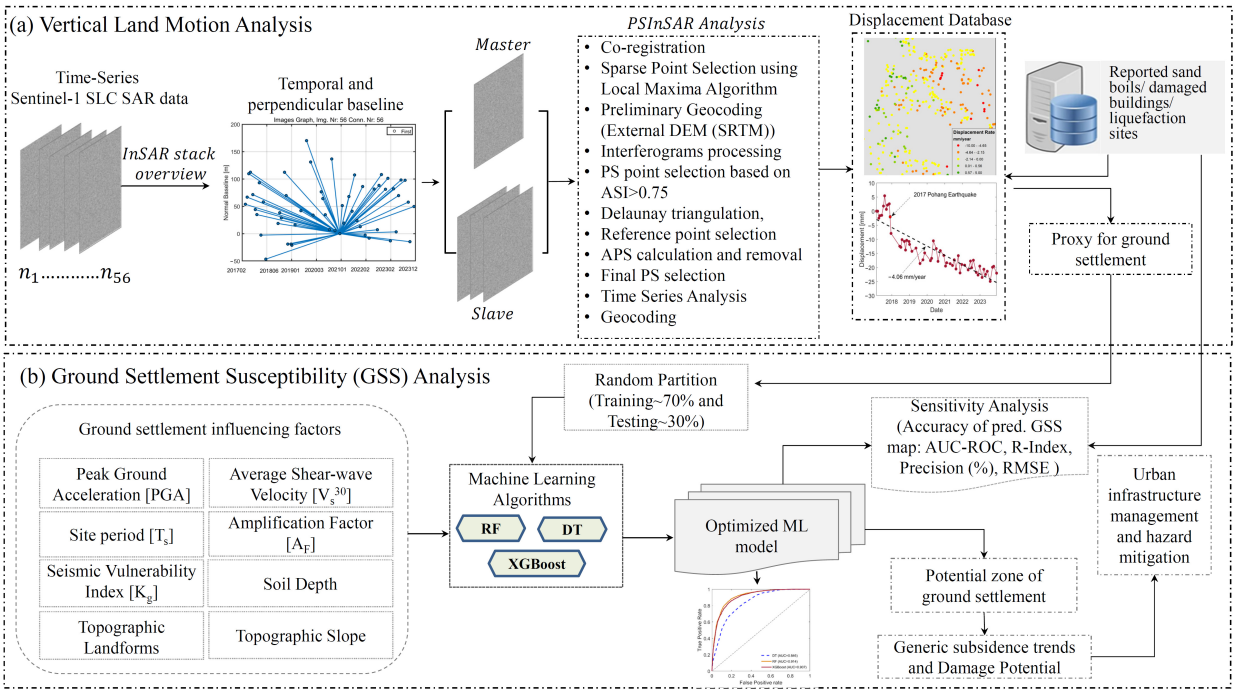

Figure 2. Methodological framework illustrating the integration of PSInSAR-derived VLM with ensemble ML approaches for GSS analysis and independent model validation.

3.1. Data

In the present study, we integrate multi-source datasets to assess GSS in the Pohang region, South Korea (Figure 2). A total of 56 Sentinel-1 Single Look Complex (SLC) images acquired in ascending mode from February 2017 to December 2023 were downloaded from the ESA Copernicus Open Access Data Hub (https://dataspace.copernicus.eu/, accessed on 27 March 2024) and used to monitor ongoing ground displacement. The selected large Sentinel-1 dataset minimizes temporal decorrelation, enabling dense extraction of coherent scatterers across urban and semi-urban environments [63]. All scenes were collected in VV polarization under the Interferometric Wide (IW) swath mode, which provides a ground resolution of ~2.3 m in the range direction and ~13.9 m in the azimuth direction [64]. The IW mode utilizes the Terrain Observation with Progressive Scans (TOPS) strategy to mitigate scalloping and improve azimuth phase stability [65,66].

To characterize the factors influencing ground settlement, we incorporated seismological, geotechnical, and topographic parameters into a holistic modeling approach. We determined various site characterization parameters (viz., T_s, A_F, and K_g) using in situ SPT-based V_s^{30} data reported by Kim and Hong [67] and a topographic proxy-based approach [68] based on the established empirical relations (i.e., [69–71]). The seismological factors, e.g., PGA, were calculated using the region-specific ground motion prediction equation (GMPE) developed by Emolo et al. [72]. The soil, topographic landforms, and slope data were prepared based on the high-resolution LiDAR DEM provided by NGII and available digital soil data. The reported building damages and sand boils/liquefaction/lateral spreading data were adopted from various research (i.e., [15,17,21–23,58]). Table 1 illustrates a comprehensive summary of the datasets used in this study, along with their corresponding sources.

Table 1. List of datasets used in the present study.

Data	Sources	Remarks
Sentinel-1SLC ascending orbit data	https://dataspace.copernicus.eu/ (accessed on 27 March 2024)	Multi-temporal SLC Data (total images = 56), acquired between February 2017 and December 2023; Incident angle ~39.2243°
Building Inventories	NSDI (Korea National Spatial Data Infrastructure)	Building footprints
Digital Elevation Model (DEM)	National Geographic Information Institute (NGII); USGS	5 × 5 m LiDAR DEM; 90 m SRTM DEM
Soil Depth	Korea Rural Development Administration (KRDA)	Digital soil map
Geotechnical Data	Kim and Hong [67]	In situ effective shear wave velocity (V_s^{30}) distribution
Regional Site Class Map	https://earthquake.usgs.gov/data/vs30/ (accessed on 15 August 2025)	Topography gradient-based V_s^{30}
Liquefaction/sand boils/lateral spreading Sites	Gihm et al. [15]; Kim et al. [22]; Kang et al. [23]; Seon et al. [58]	Surface manifestations of Liquefaction/sand boils/lateral spreading due to the 2017 Pohang earthquake
Reported building damaged	Kim et al. [21]	Building damage caused by the 2017 Pohang earthquake

3.2. Methodology

3.2.1. PSInSAR-Based Vertical Ground Displacement Analysis

PSInSAR is a multi-temporal InSAR technique that measures ground deformation at millimeter precision by analyzing the phase stability of coherent radar targets, known as Persistent Scatterers (PSs), across large SAR acquisition stacks [73,74]. Unlike conventional DInSAR, which is highly sensitive to temporal and spatial decorrelation, PSInSAR isolates stable reflectors whose phase histories remain coherent over time, thereby allowing for the accurate retrieval of time-series displacements in both urban and non-urban environments. In PSInSAR, the total interferometric phase component (φ) is decomposed into multiple components [2,75,76], as follows:

$$\varphi_{ij} = \varphi_{defo} + \varphi_{topo} + \varphi_{atm} + \varphi_{dec} \quad (1)$$

where φ_{defo} is the interferometric phase attributable to surface displacement along the radar Line of Sight (LOS), φ_{topo} represents the residual terrain phase, φ_{atm} denotes atmospheric phase delay, and φ_{dec} accounts for noise and decorrelation effects. The analytical objective of PSInSAR processing is to isolate φ_{defo}, which directly encodes cumulative displacement [75].

Here, 56 Sentinel-1A ascending orbit SLC datasets acquired between 2017 and 2023 were processed using the PSInSAR technique in the SARPROZ SAR processing tool (https://www.sarproz.com/, accessed on 12 September 2025) [74]. The PSInSAR processing workflow adhered to standard procedures, including baseline analysis, selection of master image, co-registration of secondary images, identification of sparse points based on the local maxima algorithm, interferogram generation, estimation and removal of atmospheric phase screen (APS), and processing of sparse points and subsequent time series analysis, to estimate ground displacement, as depicted in Figure 2a [2,74,77,78]. On 12 December 2020, acquisition was selected as the master data based on temporal distribution, perpendicular baseline minimization, and overall coherence optimization (depicted in the star graph in Figure 2a). Thereafter, the study area, encompassing the Pohang region, was defined as the region of interest. All slave scenes were precisely co-registered to the master image with sub-pixel accuracy using the Enhanced Spectral Diversity algorithm [79].

This approach enables the generation of N-1 interferograms from a stack of N SAR acquisitions by employing a single master–slave configuration. Differential interferograms were subsequently generated using the SRTM DEM (90 m resolution) to mitigate orbital errors, flat-Earth distortions, and remove residual topographic phase effects, ensuring accurate representation of surface deformation [80,81]. Thereafter, we utilized an amplitude stability index (ASI) of greater than 0.75 to identify the initial PS candidates [73,82]. Consequently, deformation parameters, including velocity and residual elevation, were estimated via the periodogram method within ±100 mm/year and ±100 m constraints, using a Delaunay triangulation-based spatial network [2,73,77]. We utilized a stable reference point, based on high temporal and spatial coherence, to calculate absolute displacement values by integrating all estimations [73,77,83]. Subsequently, spatio-temporal filtering (low-pass in space, high-pass in time) was applied to estimate and mitigate APS effects, enhancing phase coherence and reducing tropospheric noise [77]. To increase PS density, a second iteration was conducted using a reduced ASI threshold (greater than 0.65) [84,85]. The final APS correction was then applied using the same reference point and parameter settings adopted during APS estimation [2,78]. Thereafter, time-series analysis was performed to estimate LOS displacement, cumulative displacement, and LOS velocity. PS points with temporal coherence < 0.70 were excluded to refine the dataset further, ensuring higher confidence in displacement estimation. The detailed implementation of the PSInSAR technique has been described in [74,77,78,81], and [82].

In the present study, we utilize ascending-orbit Sentinel-1 SLC data to estimate vertical land motion (VLM). Descending-track Sentinel-1 SLC data with a sufficiently long and continuous temporal baseline were not available for the entire observation period in the study area. Therefore, a complete 3D decomposition of LOS displacement vectors could not be performed [86]. To address this limitation, we projected LOS deformation onto the vertical component, assuming negligible horizontal motion, in accordance with standard practice in subsidence-dominated InSAR applications [81,82,87]. This assumption is well supported in South Korea, where numerous investigations (e.g., [2,24,77]) consistently demonstrate that ground deformation is primarily vertical, driven by sediment compaction, groundwater withdrawal, and consolidation of reclaimed ground. Therefore, given the predominantly vertical deformation regime in reclaimed coastal and alluvial settings, where settlement is controlled by consolidation and liquefaction of unconsolidated sediments (as observed during the Pohang earthquake), LOS displacements (d_{LOS}) were converted into VLM by utilizing radar incidence angle (β) [5,77,88].

$$VLM = \frac{d_{LOS}}{\cos(\beta)} \quad (2)$$

This approach aligns with established methodologies in InSAR-based VLM studies, particularly in areas where anthropogenic activities are the primary drivers of ground deformation [87,89].

3.2.2. Influencing Factor Analysis (Geotechnical, Seismological, and Topographical)

The 2017 Pohang earthquake demonstrated that moderate events can induce severe ground deformation and infrastructure damage when compounded by unfavorable subsurface conditions, highlighting the importance of GSS mapping in enhancing seismic resilience [15,21]. The most affected zones were underlain by Quaternary alluvial and basin-fill deposits, creating ideal conditions for liquefaction, pore-fluid escape, and post-liquefaction settlement. Numerous post-event investigations identified liquefiable layers, soft-sediment deformation, and strong site amplification as the primary mechanisms driving observed failures [16,90]. Areas characterized by low $V_s{}^{30}$ and thick sedimentary cover

exhibited resonance and amplification effects that spatially coincided with sand boils, lateral spreading, and building damage [20]. Field evidence, including vertical water-escape conduits and deformed stratification, confirmed a genetic linkage between shallow liquefaction and surface settlement [15]. These findings emphasize that local site conditions, rather than seismic magnitude alone, govern the spatial variability of damage intensity. Consequently, detailed subsurface characterization becomes indispensable for reliable GSS assessment and urban risk mitigation.

Given this, robust subsurface characterization is crucial in geotechnical engineering to quantify the parameters that control ground settlement. Conventional geotechnical and geophysical tests, although precise, are spatially limited and insufficient for regional-scale assessment. Therefore, in this study, site characterization parameters were derived by integrating in situ reported geotechnical data with geospatial proxies on a big-data platform (Figure 2b). We utilized in situ SPT-based $V_s{}^{30}$ data reported by Kim and Hong [67], who developed a nationwide $V_s{}^{30}$ model for South Korea using 175,619 boreholes and H/V spectral analyses from 20 seismic stations, providing crucial input for seismic design and building code implementation. From this dataset (i.e., [67]), 1795 $V_s{}^{30}$ observations within and around the Pohang region, along with the interpolated $V_s{}^{30}$ distribution derived through the kriging method, were used (Figure 3a). However, due to data clustering and sparse coverage of the in situ $V_s{}^{30}$ data in the northern region, we further utilized the topographic proxy based $V_s{}^{30}$ model by Wald and Allen [91] (Figure 3b). Numerous studies [68,92] have demonstrated that topographic slope effectively captures lithological hardness, weathering intensity, and fracture density, all of which correlate with V_s and, thus, influence ground response. The topographic approach also offers high-resolution spatial continuity, making it particularly valuable in areas where dense borehole data is lacking.

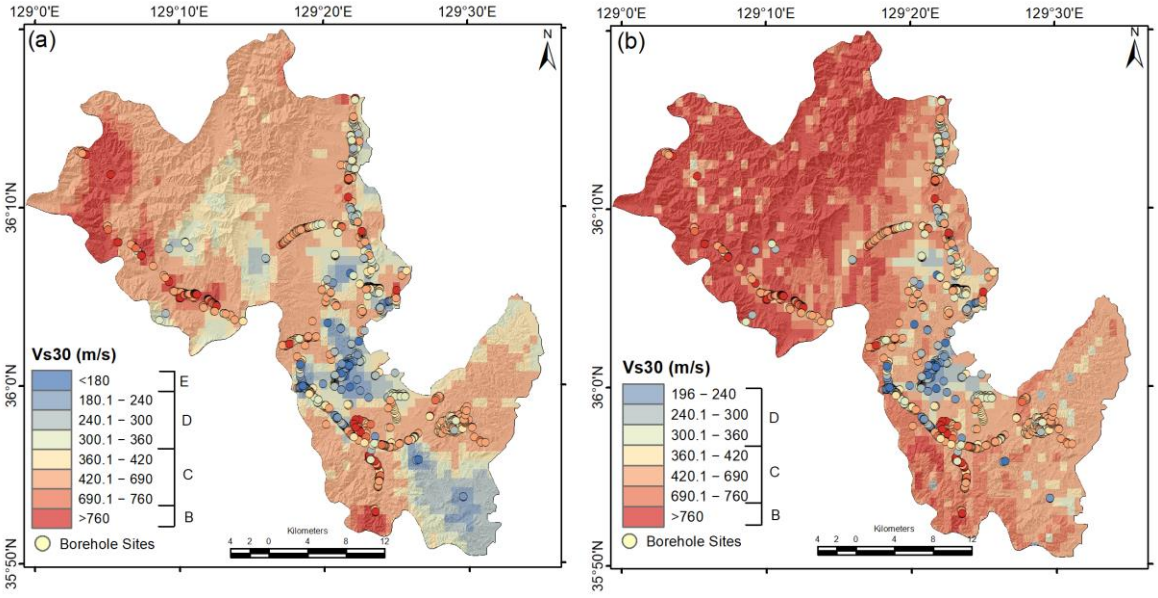

Figure 3. Spatial distribution of different site classes (i.e., E–B) in the study region based on (**a**) in situ SPT-based $V_S{}^{30}$ distribution (in situ $V_s{}^{30}$ data adapted from Kim and Hong [67]), and (**b**) topography proxy-based $V_S{}^{30}$ distribution (obtained from https://earthquake.usgs.gov/data/vs30/, accessed on 15 August 2025).

Numerous researchers have utilized various geostatistical frameworks to estimate $V_s{}^{30}$ in data-scarce regions (e.g., [93–95]). In this study, we adopted an integrated approach combining directly measured $V_S{}^{30}$ values with topography gradient-derived $V_S{}^{30}$ to achieve a refined and spatially continuous characterization of seismic site conditions across

the Pohang region. Figure 4a illustrates the histogram of logarithmic residuals between observed $V_s{}^{30}$ and those predicted using the topographic gradient approach. The residuals cluster around zero, indicating that the method provides an unbiased regional estimate, though localized deviations persist due to lithological heterogeneity and variations in sediment thickness. To overcome these limitations, both datasets were merged with greater weight on in situ data and were spatially interpolated using the IDW approach to generate a hybrid $V_S{}^{30}$ surface. Figure 4b shows the scatter plot comparison between in situ and hybrid-predicted $V_S{}^{30}$ values, which exhibits a strong linear correlation, with most data points aligning closely along the 1:1 reference line and falling within established site classification boundaries (i.e., E, D, C and B). This agreement underscores the effectiveness of the hybrid approach in mitigating bias and enhancing predictive performance, particularly in hilly terrain where direct observations are scarce. The resulting hybrid $V_S{}^{30}$ distribution (Figure 4c) provides a more spatially consistent and geologically constrained representation of site conditions across the Pohang region. Subsequently, the improved $V_s{}^{30}$ data were used to derive dynamic soil parameters (i.e., general site amplification (A_F), site period (T_s), and seismic vulnerability index (K_g)), which serve as critical inputs for GSS assessment.

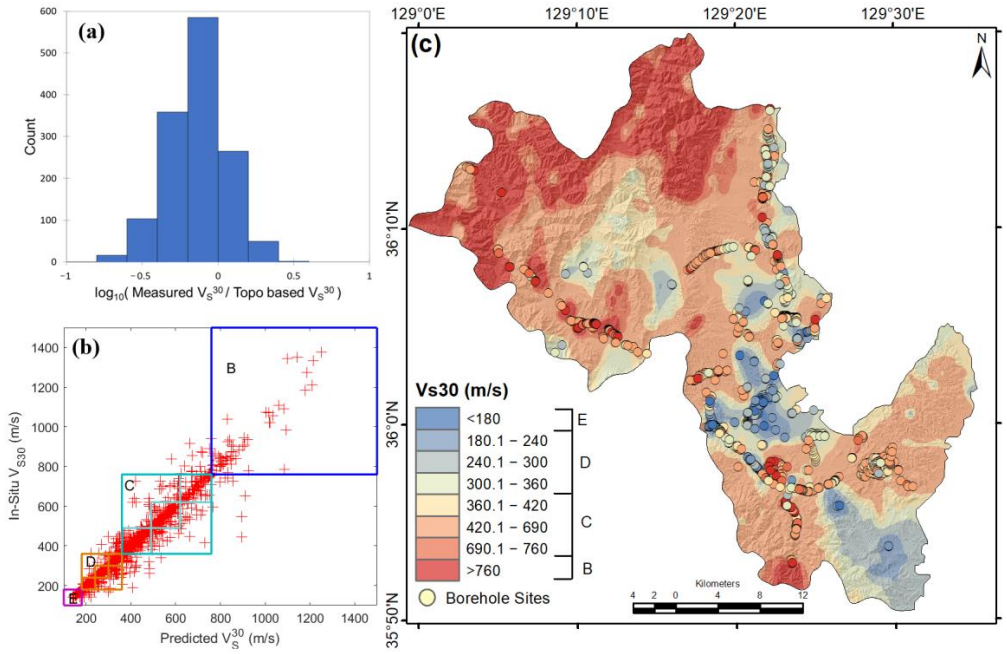

Figure 4. (**a**) Histogram of logarithmic residuals between measured $V_S{}^{30}$ and topography gradient-derived $V_S{}^{30}$, (**b**) scatter plot comparing in situ measured $V_S{}^{30}$ and hybrid interpolated $V_S{}^{30}$ values, with most points aligning along the 1:1 line and within defined site-class boundaries (i.e., E–B), and (**c**) hybrid $V_S{}^{30}$ distribution map of the study region.

Consequently, in the present study, site response parameters, including A_F, T_s, and K_g, were derived using the hybrid $V_S{}^{30}$ model based on established empirical formulations adopted from various research sources (e.g., [69–71]). Here, the general amplification factor (A_F) was computed following Borcherdt [96] as the ratio between the reference rock velocity (V_0 = 1130 m/s) and the site-specific effective $V_S{}^{30}$ of each pixel, assuming comparable rock and soil densities, without considering ground-motion levels. The reference velocity (V_0) was derived as the mean of the lower and upper bounds of rock site class B shear-wave velocities [69], with limits of 760 m/s and 1500 m/s, respectively, yielding an average of approximately 1130 m/s. Accordingly, A_F is expressed as [69], $A_F = \frac{V_0}{V_s{}^{30}}$. The estimated A_F values range from 1.0 to 9.1 (Figure 5a), and the spatial distribution is very consistent with the alluvium deposit of the region. The predominant site period (T_s) was derived from the first-mode resonance of soil deposits [69], expressed as $T_s = 1/f_0$, where $f_0 = V_S{}^{30}/4\,H$, with

the soil depth constrained to 30 m, following NEHRP standards [97]. Spatial patterns reveal short periods (0.096–0.29 s) in elevated terrains with thin overburden and longer periods (0.3–0.88 s) in low-lying alluvial zones, highlighting localized site amplification potential (Figure 5b). To account for frequency-dependent effects, the Square Root Impedance (SRI) approach [71,98,99] was utilized, as follows:

$$A_{(f)} = exp(-\pi k_o f)\sqrt{\frac{\rho^r v^r}{\rho^s v^s}} \quad (3)$$

where $A_{(f)}$ represents the amplification function, rock and soil density is assumed as ρ^r = 22 kN/m^3, ρ^s = 16 kN/m^3) [71], v^r = 1130 m/s is the average bedrock $V_S{}^{30}$, v^s is the average V_s within the upper 30 m soil profile (i.e., $V_S{}^{30}$), f denoted characteristic site frequency, and the kappa factor (0.0035) was considered following Boore and Joyner [100]. Subsequently, the amplification factor for PGA (i.e., 100 Hz) was estimated for the study region.

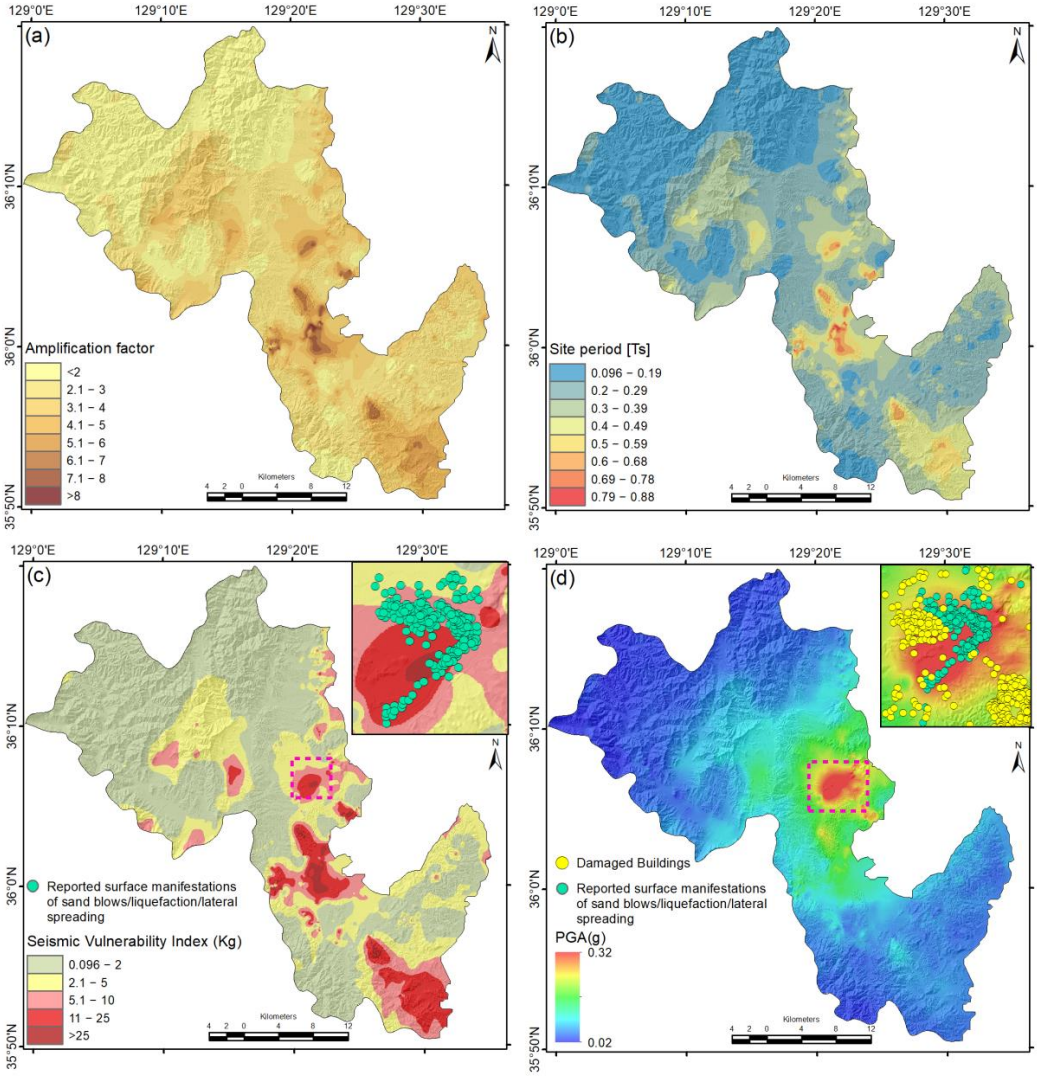

Figure 5. Geotechnical and seismological factors of the study region considered for GSS modeling (**a**) general site amplification (A_F), (**b**) site period (T_s), (**c**) seismic vulnerability index (K_g), and (**d**) PGA distribution (note: surface manifestations of sand blows/liquefaction/lateral spreading adapted from [15,23,58]; damaged buildings data were adapted from [21]).

The seismic vulnerability index (K_g), a proxy for potential damage severity [101], was calculated as $K_g = AF^2/f_0$ [70]. Numerous researchers have documented that severe ground

deformations are typically associated with K_g values greater than 15, while areas with low K_g values exhibit minimal or no damage [102,103]. Singh et al. [104] found that liquefied zones generally exhibit higher K_g values than adjacent non-liquefied areas. Furthermore, several studies have also suggested a threshold of $K_g > 5$ for liquefaction potential [105]. Figure 5c shows the spatial distribution of K_g values, ranging from 0.96 to 74.18, with areas exceeding the critical value ($K_g > 5$) coinciding with reported sand boil sites, corroborating their susceptibility to liquefaction and ground settlement.

To incorporate the seismic loading component into the GSS model, we calculated scenario-based PGA for the 2017 Pohang earthquake based on the Korea-specific next-generation ground motion prediction equation (NGA) developed by Emolo et al. [72]. The earthquake source parameters were obtained from the NECIS earthquake catalog (https://necis.kma.go.kr, accessed on 20 August 2025) and subsequently used in the reference NGA model of Emolo et al. [72]. We specifically selected this NGA model due to its robust reliability in the near-source region. Thereafter, we calculated the scenario-based PGA and convoluted it with the time-dependent (i.e.,100 Hz) amplification factor ($A_{(f)}$) to incorporate the site effect. The calculated PGA values varied from 0.02 g to 0.32 g, as depicted in Figure 5d. It was observed that most of the damage distribution was concentrated in high PGA values. Although the distribution pattern of calculated PGA agrees well with the earlier reports (i.e., [18,21,52]), differences in absolute PGA values arise from the use of a single NGA model. These scenario-based PGA estimates were subsequently incorporated into the GSS model to represent the seismic hazard component in the GSS assessment.

Topographic, geomorphological, and soil thickness parameters are incorporated as additional predictors to better constrain the susceptibility to ground settlement. The topographic slope and landform classes are determined based on a high-resolution (5 m × 5 m) DEM provided by the NGII, processed using SAGA GIS (https://sagagis.com/, accessed on 20 August 2025). The results indicate that thick alluvial deposits are concentrated in areas with slopes < 5° (Figure 6a), where gentle gradients promote sediment accumulation but complicate ground stability. Landform classification further reveals that basin interiors are dominated by plains and open slopes (Figure 6b), settings that are not only geologically underlain by soft Quaternary alluvium but also subjected to anthropogenic stresses such as groundwater extraction, urban development, and industrial expansion, factors that can accelerate subsidence [15,18,19,22]. In contrast, the northern and southern sectors are characterized by local and mid-slope ridges, which, owing to their elevated position and consolidated lithology, generally exhibit greater resistance to settlement [106]. Numerous studies have highlighted that geomorphic units, such as river channels, floodplains, deltas, paleo-river beds, lacustrine deposits, colluvium, loess, dunes, and reclaimed land, are highly susceptible to liquefaction, whereas terraces, hills, and mountains are comparatively resistant [107,108]. These observations, along with previous evidence, indicate a strong relationship between the geomorphic setting and the liquefaction potential in the Pohang region.

Additionally, soil depth data obtained from the Rural Development Administration (RDA) (http://nationalatlas.ngii.go.kr/, accessed on 25 August 2025) is classified into the following four categories: <20 cm, 20–50 cm, 50–100 cm, and >100 cm (Figure 6c). Shallow soil outcrops (<20 cm) tend to provide limited capacity for dissipating seismic energy, while deeper soil layers (>100 cm) in alluvial environments amplify ground shaking and settlement potential [109]. These factors, consistent with liquefaction-prone geomorphic settings, underscore the role of slope, landform, and soil thickness in amplifying settlement hazards. Thus, integrating slope, landform, and soil depth captures critical topographic and stratigraphic controls, enabling a more realistic representation of GSS in the Pohang basin.

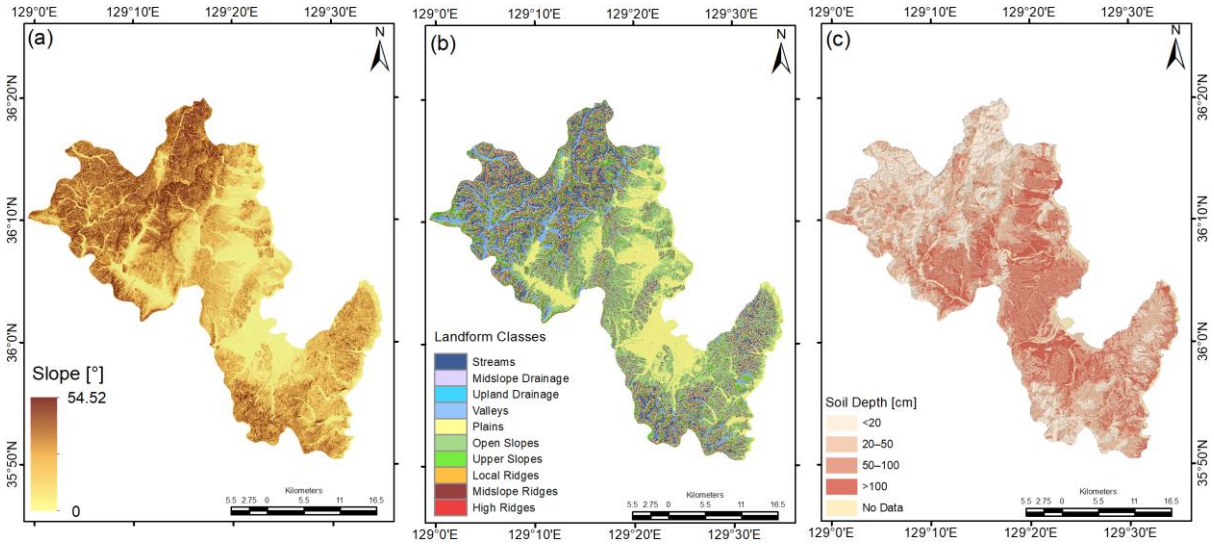

Figure 6. Topographic and geomorphological factors considered for GSS modeling: (**a**) slope, (**b**) landform classes, and (**c**) soil depth distribution.

3.2.3. Ground Settlement Susceptibility Analysis Using ML Models

Recent advances in geospatial analysis have demonstrated that integrating InSAR-derived deformation with multiple conditioning factors through ML significantly improves geohazard susceptibility modeling [43,46–51,110,111]. In this study, GSS was evaluated by integrating PSInSAR-derived VLM (dependent variable) with key independent geotechnical, seismological, and topographical factors using the following three tree-based ML algorithms: Random Forest (RF), Decision Tree (DT), and Extreme Gradient Boosting (XGBoost) (Figure 2b). These models were selected due to their robustness against multicollinearity, a prevalent issue among geotechnical variables, and their capability to model nonlinear, high-dimensional interactions without the need for feature independence or dimensionality reduction [112–114]. Subsequently, a comprehensive geospatial database was constructed, including variables such as PGA, A_F, T_s, $V_s{}^{30}$, K_g, soil depth, slope, and landform classes. The dependent variable was derived from the PSInSAR vertical displacement rates, considering only PS points with high temporal coherence (greater than 0.7). PS points with negative VLM values (VLM < 0), indicating measurable subsidence, were classified as subsiding points (class 1), whereas PS points with stable or positive VLM (VLM $\geq$ 0) values were labeled as non-subsiding class (class 0). Furthermore, to reduce spatial bias and maintain a balanced dataset, additional non-subsiding points located more than 100 m from subsiding PSs were included. This binary settlement indicator was then spatially linked with all geotechnical, topographic, and seismological predictors to construct the inputs for training and testing ML models. The dataset was subsequently split into training (70%) and testing (30%) sets following established protocols [115]. This approach ensured that the dependent variable captured meaningful deformation behavior grounded in both the InSAR observations and the site conditions.

Among the selected algorithms, DT provides interpretable rule-based classifications through recursive partitioning of the feature space, using information gain measures such as the Gini index or entropy [116,117]. RF enhances model stability and generalization by aggregating multiple decision trees through bootstrap aggregation (bagging), mitigating overfitting and enabling variable importance ranking [53,118]. XGBoost further advances this ensemble paradigm using gradient boosting, where weak learners are iteratively optimized to minimize residual errors from prior models and prevent overfitting [119]. The combined use of these three models provides a methodological balance between interpretability, stability, and feature ranking, resulting in a superior predictive performance

and ensuring a comprehensive evaluation of GSS. Therefore, by comparing these models, the study ensures both interpretability and predictive strength, thereby generating a reliable GSS map to support urban infrastructure risk management and disaster mitigation.

3.2.4. Model Validation

The predicted GSS index was validated using a two-step approach. The ML models were first trained and tested on PSInSAR-based VLM data. Subsequently, the optimized susceptibility model was compared against independent field-based reported damage databases. The performance of the three ML models was evaluated using accuracy, precision, recall, F1-score, and the area under the receiver operating characteristic curve (AUC-ROC) [49,51,53]. The AUC-ROC quantified each model's ability to distinguish between subsidence and non-subsidence areas, independent of classification thresholds [51]. Additionally, recall, precision, accuracy, and F1-score were calculated to assess class-specific performance, which is particularly important given the class imbalance [53,120].

The optimized ML model-based GSS map was validated against field evidence from the 2017 Pohang earthquake, including sand boils, fissures, and reported structural damage. We prepared an extensive field evidence-based database of reported building damages and sand boils/liquefaction/lateral spreading, compiled from various research sources (e.g., [15,21–23,58]). Thereafter, the MAE, MSE, and RMSE were used to analyze the effectiveness of the final GSS map. The RMSE and MSE measure the forecasting errors of the model, whereas the MAE measures its generalization error [115]. Furthermore, we utilized density (Di), precision (P), and the R-index to assess the accuracy of the final GSS map [115,121]. The RMSE, MAE, and MSE were determined using the following Equations (4)–(6):

$$RMSE = \sqrt{\frac{1}{n}\sum_{i=1}^{n}\left(S_{obs} - S_{pre}\right)^2} \quad (4)$$

$$MAE = \frac{1}{n}\sum_{i=n}^{n}\left|\left(S_{obs} - S_{pre}\right)\right| \quad (5)$$

$$MSE = \frac{1}{n}\sum_{i=n}^{n}\left(S_{obs} - S_{pre}\right)^2 \quad (6)$$

where S_{obs} denotes the observed ground settlement (i.e., liquefaction, lateral spreading, structural damage, and sand boils), S_{pre} is the calculated GSS values, and n represents the total damage dataset.

The final GSS zonation map (GSSM) validation was further performed by examining the relationship between the existing damage events and GSS zones based on the R-index analysis and the precision parameter. The R-index evaluates the concentration of observed damage events within each susceptibility class and was computed following Equation (7) [115,121],

$$R = \left({}^{n_i}/_{N_i}\right)/\sum\left({}^{n_i}/_{N_i}\right) \times 100 \quad (7)$$

where n_i represents the number of damage events located within a given GSS zone, while N_i represents the total pixels (or areas) belonging to that same GSS zone. A higher R-index indicates a stronger correspondence between observed damage and predicted susceptibility. Furthermore, the precision (P) parameter is widely used to validate the predicted geohazard susceptibility zones. Thus, the precision of the predicted GSS zonation map was determined using Equation (8) [122],

$$P = D_{hs}/D_T \quad (8)$$

where D_{hs} represents the number of damage sites situated within the high to very high GSS zone, and D_T represents all damage sites in the study region. This combination of internal (AUC-

ROC) and external (field-based) validation ensures the reliability of the optimized susceptibility map, which identifies high-risk areas while demonstrating strong predictive performance.

4. Results

4.1. Spatial Distribution of PSInSAR-Derived VLM

The PSInSAR analysis of 56 Sentinel-1 SLC images, spanning from February 2017 to December 2023, successfully quantified long-term ground deformation across the Pohang region. The results revealed heterogeneous settlement patterns, with VLM rates ranging from −10 mm/year to 4.89 mm/year and an average VLM of −1.05 mm/year (Figure 7a). The most pronounced subsidence was concentrated in reclaimed areas, industrial complexes along the Hyeongsan River, and low-lying urban districts underlain by unconsolidated Quaternary deposits. These areas correspond to geotechnically weak deposits characterized by thick unconsolidated soils and high site amplification potential. In contrast, the surrounding hills underlain by granitic and metamorphic rocks exhibited negligible deformation, confirming the geological control on settlement processes. On the other hand, Figure 7b illustrates the spatial distribution of PSInSAR-derived subsidence rates (only negative VLM PSs) across the study area, with an average rate of −1.57 mm/year, highlighting their relationship with the 2017 Pohang earthquake building damage sites. It was observed that most earthquake-induced building damage sites (green dots, zoomed boxes) are clustered within or adjacent to high-subsidence zones delineated by the PSInSAR analysis.

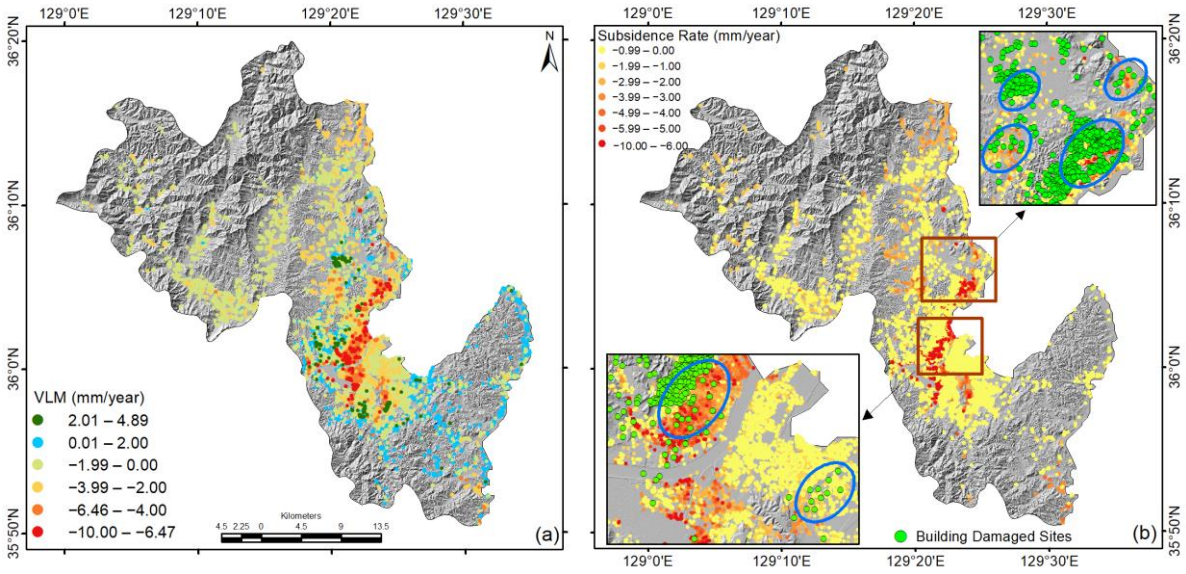

Figure 7. (**a**) Spatial distribution of PSInSAR-derived VLM and (**b**) subsidence rate map overlaid with building damage sites from the 2017 Pohang earthquake, illustrating a strong spatial correspondence between zones of high subsidence and damaged structures (note: the spatial distribution of damaged building data adapted from Kim et al. [21]).

To understand the pre- and post-seismic deformation behavior in the Pohang region, time-series analyses of PSInSAR-derived ground displacement were performed for sites located near the 2017 earthquake-induced sand boil zones (Figure 8). The temporal displacement profiles from six representative sites (Figure 8a–f) reveal consistent and progressive subsidence following the earthquake, with deformation rates ranging from −0.66 mm/year to −4.08 mm/year. These results indicate that vertical ground displacement persisted well beyond the mainshock, implying that post-seismic consolidation and groundwater-related compaction are the dominant mechanisms governing ongoing settlement. Spatial correlation between zones of higher subsidence and reported structural damage further

substantiates the persistent deformation response of loose, water-saturated sediments to seismic loading. The gradual yet continuous downward displacement underscores the long-term instability of reclaimed and unconsolidated deposits, highlighting the need for sustained geotechnical monitoring and subsurface reinforcement in vulnerable urban areas. Therefore, the PSInSAR-derived deformation patterns confirm that the 2017 Pohang earthquake not only induced instantaneous coseismic settlement, but also prolonged post-seismic subsidence, reflecting the coupled effects of seismic excitation, lithostratigraphic heterogeneity, and hydrological processes. This strong spatial coherence between measured deformation and observed damage validates the reliability of PSInSAR-derived VLM as a physically meaningful input for the ML-based GSS modeling framework.

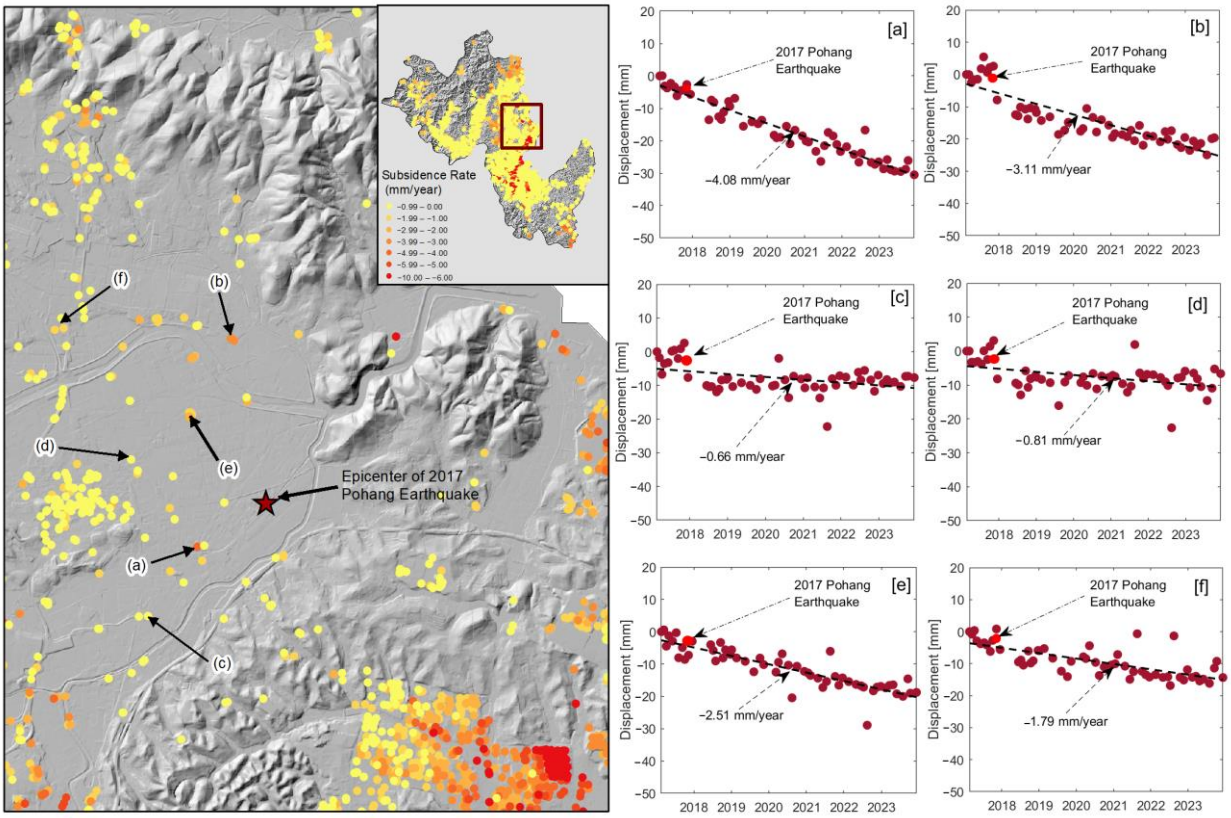

Figure 8. Ground subsidence (negative VLM PSs) in the epicentral region of the Pohang earthquake derived from the PSInSAR analysis (left panel). The right panel shows the temporal evolution of pre- and post-earthquake vertical displacement at six representative sites (**a**–**f**) located in and around areas affected by liquefaction/sand boils/lateral spreading following the earthquake (Figure 1c).

4.2. Ground Settlement Susceptibility (GSS) Mapping

In the present study, we utilized three machine learning algorithms (i.e., RF, DT, and XGBoost) to quantify the relative influence of eight settlement-controlling factors, i.e., V_s^{30}, site period (T_s), site amplification (A_F), seismic vulnerability index (K_g), peak ground acceleration (PGA), soil depth, slope, and landform, on ground settlement susceptibility in the Pohang region. The variable importance analysis (Figure 9) elucidates the governing geotechnical and seismological mechanisms underlying post-seismic settlement behavior. Across all models, topographic slope and PGA consistently emerged as the dominant predictors, reflecting the coupled control of geomorphic gradients and seismic loading intensity on settlement amplification. The significance of landform classification further highlights the vulnerability of reclaimed and low-lying coastal plains, where unconsolidated alluvial deposits are prone to differential compaction and liquefaction-induced subsidence. In addition, moderate contributions from T_s and K_g indicate that resonance

and site amplification effects modulate deformation intensity, especially within thick, soft sedimentary sequences. Soil depth also exerts a secondary influence, implying that thicker alluvial layers facilitate greater post-seismic consolidation settlement. Among the models, RF and XGBoost, both ensemble-based frameworks, captured more geotechnically consistent relationships, effectively modeling nonlinear interactions and hierarchical dependencies among variables. In contrast, the DT model exhibited a simplified attribution pattern, overemphasizing individual predictors due to its single-split decision structure. Thus, the ensemble approaches provide a more comprehensive and physically coherent representation of the interplay between seismic excitation, soil mechanical behavior, and topographic configuration. These findings highlight the substantial influence of seismic loading intensity and terrain morphology on ground settlement in the Pohang region.

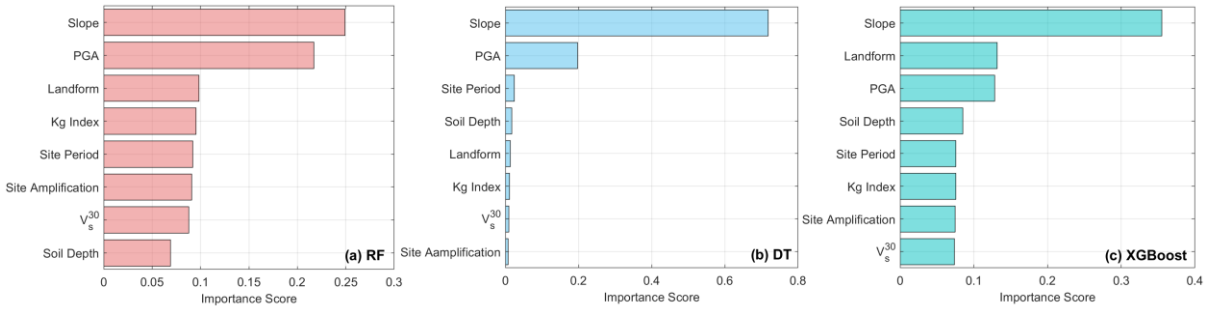

Figure 9. The relative importance of settlement-influencing factors derived from (**a**) the RF model, (**b**) the DT model, and (**c**) the XGBoost model.

The predictive performance and generalization ability of the three ML models (i.e., RF, DT, and XGBoost) were evaluated using PSInSAR-based VLM data and independent in situ reported damage and ground settlement (i.e., liquefaction, lateral spreading and sand boil) sites. Table 2 presents a comparative analysis of the training and testing dataset results for all three models, providing insights into the generalization performance of each model. The generalization assessment indicates that RF achieved the highest overall performance, with an average accuracy of 91.6% and the smallest gap (0.4%), reflecting excellent consistency between training and testing. XGBoost also performed strongly (average 91.2%) but showed a slightly larger gap (0.9%), suggesting mild overfitting. In contrast, DT exhibited the lowest accuracy (84.1%) despite a moderate gap (1.2%), which highlights its limited predictive ability. RF and XGBoost demonstrated strong generalization, with RF being the most stable; however, DT underperformed in both the training and testing phases. These performance differences stem from the inherent strengths of ensemble learning. RF reduces variance through bootstrap aggregation (bagging), where multiple decorrelated trees are trained on randomized subsets of the data and features [118]. This aggregation stabilizes predictions and limits overfitting, which is critical when modeling spatially variable geotechnical and seismological environments. XGBoost, on the other hand, relies on gradient boosting, where each tree is built sequentially to correct the residual errors of previous learners [119]. This procedure reduces bias and enhances the model's capacity to capture nonlinear dependencies and higher-order interactions among key predictors such as slope, PGA, landform class, site period, and soil depth. In contrast, a single decision tree lacks these variance and bias-reduction mechanisms and often overfits to localized patterns, making it less suited for representing the multiscale processes that control post-seismic ground deformation in reclaimed and geomorphically complex terrain. The ensemble characteristics of RF and XGBoost, therefore, provide a more robust and physically consistent framework for modeling ground settlement susceptibility.

Table 2. Generalization ability test of three ML models.

Datasets	RF_{AUC}	DT_{AUC}	$XGBoost_{AUC}$
Training	0.918	0.846	0.916
Testing	0.914	0.836	0.907
Difference (%)	0.4%	1.2%	0.9%
Average	0.916	0.841	0.912

Furthermore, the performance of the RF, XGBoost, and DT models is summarized in Table 3. Among them, RF demonstrated the highest discriminative ability with an AUC-ROC of 0.914, coupled with strong precision (0.87), recall (0.91), and F1-score (0.89) for the positive class, indicating reliable identification of susceptible areas. XGBoost followed closely with an AUC-ROC of 0.907, exhibiting a slightly lower recall and precision balance, yet still achieving a competitive accuracy (0.84). In contrast, DT exhibited the weakest performance, with an AUC-ROC of 0.836 and a notable decline in precision (0.78) and F1-score (0.85), reflecting its tendency to overpredict susceptibility. Therefore, based on the model generalization and performance comparison, the RF model was identified as an optimized model for GSS mapping of the Pohang region, highlighting its robustness in handling nonlinear relationships among geotechnical, seismological, and topographic factors.

Table 3. Performance comparison of ML models for GSS mapping.

ML Models	Accuracy	Precision	Recall	F1-Score
RF	0.85	0.87	0.91	0.89
XGBoost	0.84	0.85	0.91	0.88
DT	0.79	0.78	0.93	0.85

The ground settlement susceptibility maps (GSSMs) generated using the RF, DT, and XGBoost models delineate the spatial distribution of settlement potential across the Pohang region, as depicted in Figure 10a–c. The susceptibility index was classified into the following five distinct susceptibility zones: very low, low, moderate, high, and very high, based on an equal interval scheme to ensure consistent comparative evaluation among models. All three models exhibit a coherent spatial pattern, with Pohang's southeastern residential, industrial, and commercial parts showing the highest settlement susceptibility, corresponding closely with previously reported liquefaction and lateral spreading sites [15]. It was observed that industrial facilities in the Pohang port and steel manufacturing districts were located in areas of high settlement susceptibility, while residential clusters near the Hyeongsan River also overlapped with zones of elevated hazard, highlighting potential vulnerability to future seismic or anthropogenic triggers. These zones coincide with thick alluvial deposits, low $V_s{}^{30}$, and elevated PGA, indicating that geotechnical fragility and seismic loading intensity jointly govern post-seismic settlement behavior. The zoomed boxes (Figure 10a′–c′) show that areas mapped as "high" to "very high" susceptibility strongly coincide with reported surface manifestations of liquefaction, sand boils, and lateral spreading [15,23,58], validating the predictive reliability of the models in capturing geotechnically unstable zones. Similarly, the overlays of building damage locations (Figure 10a″–c″) indicate that the majority of damaged structures during the 2017 Pohang earthquake are located within the high- and very-high-susceptibility classes, particularly around the Heunghae basin and Yeongil Bay reclamation areas. This spatial correspondence emphasizes the practical utility of GSSMs in reflecting both subsurface deformation mechanisms and observed structural consequences.

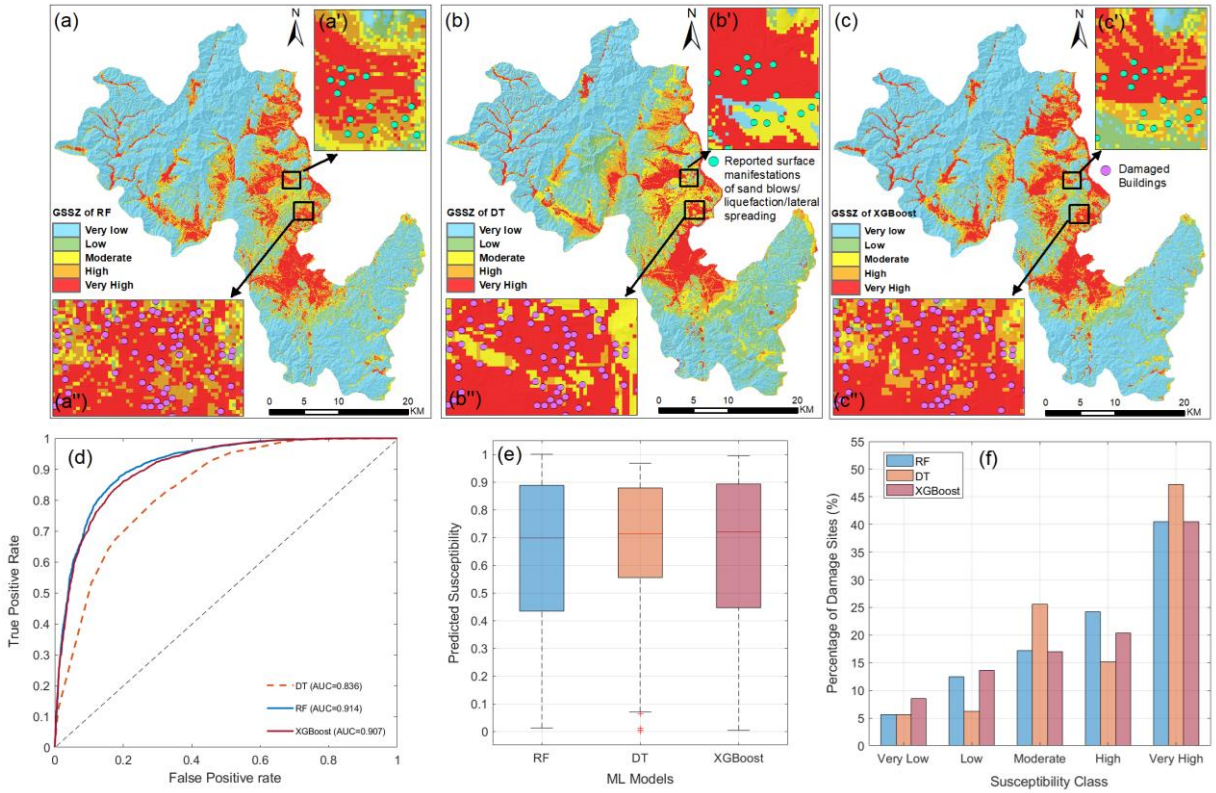

Figure 10. Ground settlement susceptibility maps of the Pohang region generated using (**a**) RF, (**b**) DT, and (**c**) XGBoost models, where insets (**a′**–**c′**) show reported surface manifestations of liquefaction, sand boil, and lateral spreading, and insets (**a′′**–**c′′**) exhibit reported damaged buildings, while (**d**) presents the ROC curves, highlighting the higher predictive performance of RF and XGBoost compared to DT, and (**e**) and (**f**), respectively, depict the distribution and percentage of observed damage sites across different susceptibility classes (note: surface manifestations of sand blows/liquefaction/lateral spreading adapted from [15,23,58]; damaged buildings data were adapted from [21]).

The model performance evaluation (Figure 10d) further substantiates these findings. The ROC curves demonstrate a strong discriminative predictive capability for the ensemble-based models (AUC = 0.914 for RF and 0.907 for XGBoost), while the single DT model achieves a lower AUC of 0.836. The higher AUC values for RF and XGBoost indicate superior generalization ability and robustness in capturing nonlinear dependencies between seismic, geotechnical, and topographic predictors. Furthermore, the boxplot analysis (Figure 10e) compares predicted susceptibility values at reported damage sites across models, showing that RF and XGBoost exhibit more compact distributions and higher median susceptibility values than DT, suggesting more stable and consistent predictions based on an independent dataset. The bar graph (Figure 10f) quantifies the percentage of reported damage sites falling within each susceptibility class, revealing that over 80% of damaged buildings correspond to moderate-, high-, and very-high-susceptibility zones for RF and XGBoost models. In contrast, DT shows greater dispersion, reflecting its lower predictive precision. These results confirm that ensemble-based approaches (RF and XGBoost) outperform the single decision tree model by effectively handling complex multivariate interactions and reducing overfitting. Thus, the derived susceptibility maps provide a scientifically validated spatial framework for assessing seismic-induced ground deformation hazards, supporting infrastructure resilience planning and post-earthquake risk mitigation in the Pohang region.

Table 4 illustrates the areal distribution of GSS zones derived from the RF, DT, and XGBoost models, which reveals notable variations in spatial prediction patterns. It is observed that all three models consistently indicate that the majority of the region is characterized by low settlement potential, with the "very low" and "low" susceptibility zones collectively encompassing over 70% of the total area. This dominance reflects the geotechnical stability of extensive inland and elevated terrains underlain by dense, less compressible soils and low seismic amplification conditions. Among the models, XGBoost predicts the largest extent of the very-low-susceptibility zone (692.32 km^2), followed closely by RF (657.83 km^2), suggesting strong generalization in identifying geotechnically stable regions. Conversely, the DT model delineates a comparatively smaller stable area (557.79 km^2) and larger moderate-to-high-susceptibility zones, revealing its tendency to overfit and oversimplify the nonlinear interactions between seismic loading and geomorphic parameters. The very-high-susceptibility zone, representing regions most vulnerable to post-seismic settlement, occupies 136.75 km^2 (RF), 133.24 km^2 (DT), and 157.44 km^2 (XGBoost), predominantly coinciding with quaternary deposits, basin fill, reclaimed coastal plains, and riverine alluvial deposits where thick unconsolidated sediments amplify ground motion and promote consolidation-induced subsidence. These spatial patterns indicate that ensemble-based models (RF and XGBoost) outperform the single-tree DT model in balancing sensitivity and specificity, producing more physically consistent susceptibility delineations that align with observed damage and PSInSAR-derived subsidence patterns. The results affirm the robustness of ensemble learning in integrating multi-source geotechnical, seismological, and topographical parameters for regional-scale GSS mapping in complex geological settings.

Table 4. Areal distribution (km^2) of GSS zones predicted by the RF, DT, and XGBoost models.

GSS Zones	Spatial Extent of Susceptibility Levels (km^2)		
	RF Model	**DT Model**	**XGBoost Model**
Very Low	657.83	557.79	692.32
Low	141.61	215.16	113.38
Moderate	101.56	150.30	78.67
High	98.69	79.94	94.62
Very High	136.75	133.24	157.44

4.3. Structural Vulnerability Assessment Based on the Optimal GSS Model

The structural vulnerability assessment was conducted using the optimal GSS map derived from the RF model, which demonstrated the highest predictive accuracy among the tested ensemble algorithms. Subsequently, the RF-based GSS map was integrated with a detailed building footprint inventory obtained from Korea's National Spatial Data Infrastructure (NSDI) within a Geographic Information System (GIS) framework. This integration enabled the quantification of building exposure across susceptibility classes and the evaluation of potential structural vulnerability under varying settlement conditions (Figure 11a,b). It was observed that ~65% of all mapped buildings were classified as highly and very highly susceptible, indicating a concentration of vulnerable assets in areas subject to ongoing or future ground deformation (Figure 11b). The close alignment between high-GSS zones and dense urbanized sectors highlights the compound hazard potential, where persistent subsidence can exacerbate the effects of seismic loading or hydrological instability. The representative displacement time series extracted from very-high-susceptibility areas (Figure 11c) shows a continuous downward trend with a VLM rate of −8.7 mm/year (R^2 = 0.95), reflecting progressive deformation that could compromise building foundations and serviceability over time. The findings highlight the urgent need for targeted risk mitigation strategies in high-susceptibility zones and provide a practical foundation for

incorporating deformation susceptibility into future urban development and building code planning in the Pohang region.

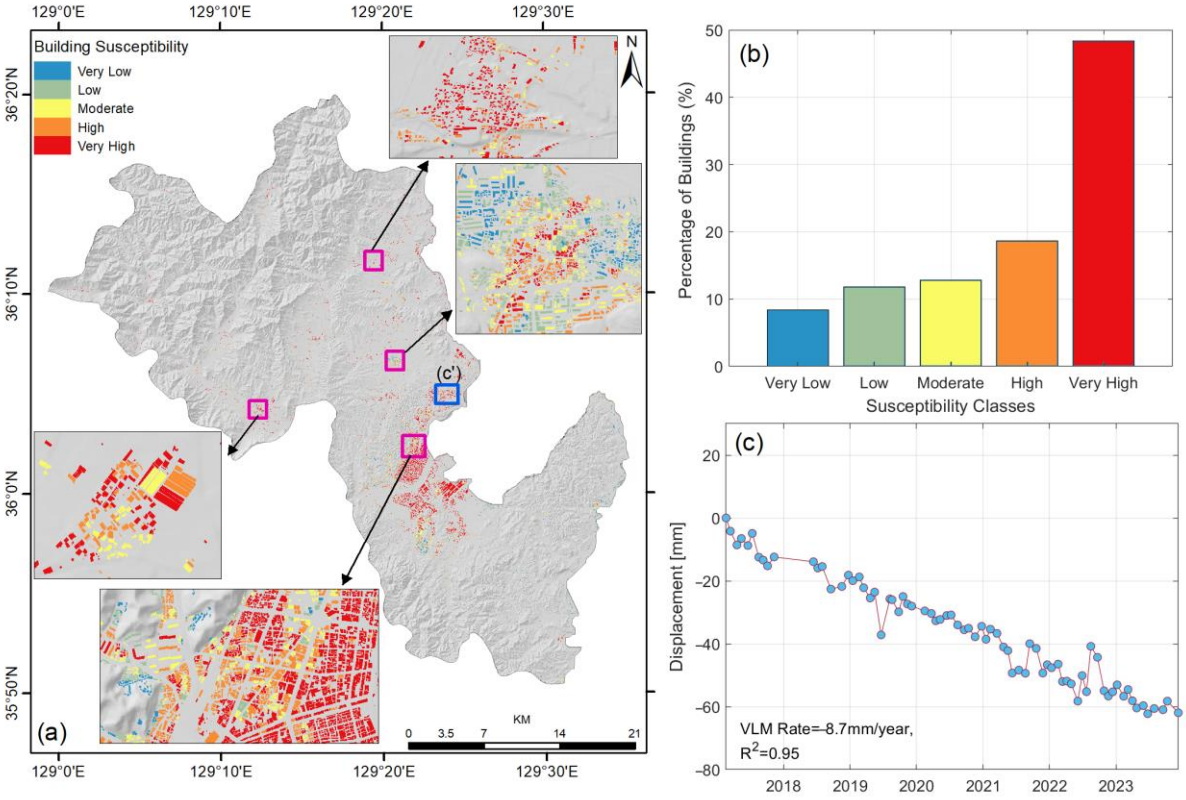

Figure 11. (**a**) Building-level susceptibility map derived based on the optimal RF-based GSS model, (**b**) distribution of buildings across different susceptibility classes, and (**c**) representative PSInSAR-derived displacement time series from a building located in a very-high-susceptibility zone (**c**').

5. Discussion

The integration of PSInSAR-derived VLM with ML modeling presents a physically consistent and technically robust framework for assessing GSSM in the Pohang region. The PSInSAR analysis of 56 Sentinel-1 SLC images (2017–2023) captured the spatial and temporal evolution of ground deformation with millimeter-level precision, directly quantifying settlement behavior across diverse geomorphic and geological environments. The derived VLM values ranged from −10 mm/year to 4.89 mm/year, with an average regional rate of −1.05 mm/year, highlighting spatial heterogeneity in deformation. Pronounced subsidence was concentrated in reclaimed coastal zones, industrial corridors along the Hyeongsan River, and alluvial plains underlain by unconsolidated Quaternary sediments characterized by high site amplification potential and low geotechnical stiffness. In contrast, regions underlain by Jurassic granite, such as the Yucheon Group and the Sindong-Hyang Group, as well as the metamorphic uplands, exhibited negligible deformation, demonstrating the strong lithological control on settlement processes.

The spatial coherence between high-subsidence zones and earthquake-induced structural damage further validates the reliability of PSInSAR observations. Most buildings damaged by the 2017 Pohang earthquake [21] are located in areas of accelerated subsidence, indicating that seismic shaking amplified deformation in geotechnically weak zones. Time-series displacement profiles (Figure 8) revealed persistent post-seismic subsidence rates between −0.66 and −4.08 mm/year, suggesting ongoing consolidation and groundwater-related compaction well beyond the mainshock. These patterns confirm that the 2017

earthquake triggered immediate ground deformation and initiated long-term settlement processes governed by coupled seismic–hydro-geotechnical interactions.

Subsequently, we utilized PSInSAR-derived VLM datasets as training and testing data for ML modeling to ensure that the GSS assessment was rooted in physically observed deformation rather than purely empirical correlations. This data-driven approach constrained model learning to reflect real-world settlement behavior, thereby enhancing both generalization and interpretability. Subsequent validation using independent evidence, such as sand blows/liquefaction/lateral spreading sites [15,23,58] and documented building damage inventories [21], provided strong external corroboration. The spatial overlap between high-susceptibility zones and reported field-observed damage confirms the predictive robustness and physical realism of the ML-based GSSM framework. Among the evaluated ML models, the ensemble algorithms, i.e., RF and XGBoost, outperformed the single-tree classifier (DT) in predictive accuracy and spatial coherence. The generalization ability tests (Table 2) revealed minimal discrepancies between training and testing AUC values, reflecting their strong capacity to capture nonlinear and multivariate relationships among seismic, geomorphic, and geotechnical parameters. Variable importance analysis consistently highlighted slope, PGA, and landform as the dominant predictors, underscoring the coupled influence of topographic stress redistribution, seismic loading intensity, and soil type variability on settlement behavior. The physical mechanisms that make slope and PGA dominant predictors for ground settlement are rooted in the interplay between gravitational forces and seismic activity. Slope influences ground settlement through gravitational instability, which is exacerbated by the thickness and composition of sediment layers [123]. On the other hand, PGA represents the intensity of ground shaking and directly controls dynamic loading during seismic events. Stronger shaking increases pore-pressure buildup, accelerates consolidation, and can trigger liquefaction in loose, water-saturated materials [124]. These processes lead to abrupt vertical settlement, lateral spreading, and post-seismic compaction. The substantial contribution of PGA in the models, therefore, reflects its role as the primary driver of seismic-induced ground failure, especially in regions where soft sediments and reclaimed deposits exhibit nonlinear responses to cyclic loading. It was observed that the RF model produced smoother and geotechnically coherent spatial patterns, while XGBoost delineated localized deformation hotspots more sharply due to its iterative boosting mechanism. Based on the superior balance between accuracy, stability, and interpretability, the RF model was identified as the optimal classifier for GSS mapping in the Pohang region.

The spatial distribution of susceptibility classes (Table 4) reveals that high- to very-high-susceptibility zones (~235–252 km^2) are predominantly located in Quaternary deposits, basin-fill areas, and riverine plains, regions with thick compressible soils and elevated groundwater levels conducive to post-seismic consolidation and lateral spreading. Notably, the 2017 Pohang earthquake epicenter lies within a very-high-susceptibility zone. Conversely, low- to very-low-susceptibility zones (~799–806 km^2) correspond to elevated, well-drained terrains characterized by higher $V_s{}^{30}$ and lower site amplification. The close alignment between model-predicted zones and independent field observations further confirms the physical validity of the integrated approach.

Further, the resulting optimal susceptibility model was validated against independent damage datasets, providing an external and spatially explicit evaluation of the model. The validation using independent field damage data confirmed the reliability of optimal RF predictions (Table 5). The sensitivity analysis revealed that high-risk zones predicted by RF captured a disproportionately large fraction of observed damage sites, with the very-high-susceptibility zone covering 12% of the predicted area (P_i) but containing 40.47% of the observed damage (O_i), reflected in increasing R-Index values across susceptibility classes.

The statistical metrics (MSE = 0.176, MAE = 0.33, RMSE = 0.419) demonstrated a close agreement between the predicted susceptibility and the observed damage. Classification accuracy using a 0.5 threshold further confirmed that RF reliably identifies susceptible areas (accuracy = 73.99%). These metrics provide a robust scientific justification for selecting RF as the optimal model for generating the GSS map, ensuring high predictive performance and reliable spatial identification of vulnerable areas.

Table 5. Validation of optimal ML model based on the independent reported damage data through different statistical metrics.

GSS Zones	P_i (%)	O_i (%)	R-Index	P	MSE	MAE	RMSE	Accuracy (Cutoff = 0.5)
Very Low	57.9	5.5	1.03					
Low	12.5	12.5	10.9					
Moderate	8.9	17.2	20.8	81.9	0.176	0.33	0.419	73.99
High	8.7	24.2	30.2					
Very High	12.0	40.47	36.4					

It was observed that the very high ground settlement susceptibility regions are mostly associated with quaternary alluvium deposits and seismic site classes E (V_s^{30} < 180 m/s) and D (V_s^{30} 180–360 m/s) (Figures 4c and 10a). The time-series displacement was strongly correlated with the reported sand boil sites that emerged after the 2017 Pohang earthquake and exhibited sudden subsidence after the event (Figure 1b,c). Further, it was observed that a higher PGA (>0.1 g) in the epicentral region was associated with very-high-susceptibility zones. Interestingly, the distribution of high- and very-high-GSS classes was consistent with the spatial distribution of the K_g index (>5) (Figures 5c and 10a), corroborating their susceptibility to liquefaction and ground settlement. Further, the cross-correlation between PSInSAR-derived subsidence data and GSS index confirmed the physical reliability of the machine learning-based GSS mapping (Figure 12). The box plots in Figure 12a reveal that the median subsidence rates progressively increase from very-low- to very-high-susceptibility zones, indicating a strong positive correlation between predicted GSS and the spatial distribution of settlement severity derived from radar interferometry. The scatter plot in Figure 12b further demonstrates a positive correlation between predicted susceptibility values and observed significant subsidence rates (i.e., VLM with <−2.5 mm/year), with the densest clustering of high VLM magnitudes (<−5 mm/year) occurring within the high- and very-high-susceptibility ranges (≥0.6). This nonlinear yet coherent relationship confirms that the model outputs are physically meaningful and responsive to settlement processes. Additionally, the frequency distribution in Figure 12c shows that approximately 70–80% of the subsiding PSs are concentrated within the high- to very-high-susceptibility zones, reinforcing the predictive robustness and spatial validity of the GSSM framework. This close agreement highlights that the PSInSAR-derived subsidence PSs effectively validate the predictive performance and spatial realism of the GSSM framework across the Pohang region. Therefore, the developed settlement susceptibility and building damage potential maps are crucial for monitoring the vulnerability of urban infrastructures, optimizing urban planning to minimize earthquake risk and preventing cascading hazards from future surface rupture.

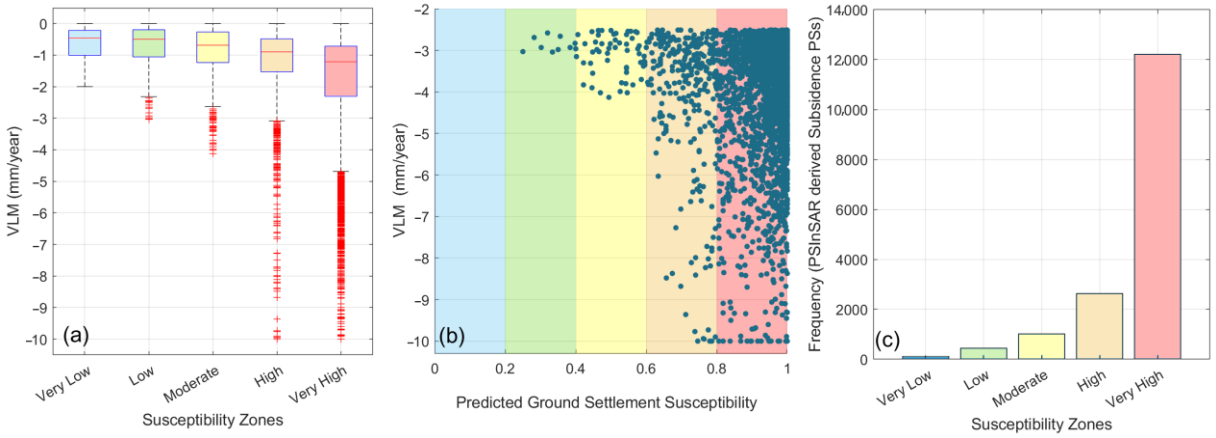

Figure 12. (**a**,**b**) Box and scatter plots showing the distribution of PSInSAR-derived subsidence PSs across different GSS classes, and (**c**) bar graph illustrating the frequency of PSInSAR-derived subsidence PSs within each GSS class.

To further characterize generic settlement behavior, displacement time series for PS points within moderate- to very-high-susceptibility classes were analyzed (Figure 13). For this purpose, we selected subsidence PSs located in moderate- to very-high-susceptibility classes and displacement time series were analyzed by fitting linear trends and calculating the coefficient of determination (R^2). To ensure the robustness of the derived trends, only subsidence PS points with an R^2 value greater than 0.6 were included, thereby minimizing the influence of noisy or poorly correlated signals. The filtered data were then averaged for each susceptibility class, and the resulting mean displacement trends were plotted for the moderate, high, and very high GSS zones (Figure 13). The mean settlement rates of −2.21 mm/year, −2.91 mm/year, and −3.21 mm/year for the moderate-, high-, and very-high-susceptibility zones, respectively, demonstrate a consistent increase in subsidence intensity with GSS class. This pattern supports the physical relevance of the machine learning-based susceptibility zoning, as higher-GSS areas correspond to zones of greater cumulative deformation. Further, the distinct characteristics of generic settlement rates exhibited that the susceptibility zones are meaningful and reflect distinct deformation behaviors. These generic settlement trends provide an empirical reference for defining foundation design tolerance levels and developing region-specific codal provisions. The resultant generic trends can help identify areas where mitigation measures, such as deep foundations, soil stabilization, or restricted development, are necessary to reduce long-term settlement risks. Moreover, integrating these trends into urban planning frameworks allows authorities to anticipate potential deformation-related hazards and guide new urbanization toward more stable ground conditions.

Although the analysis provides valuable insights into ground settlement processes, the study is subject to several constraints related to data quality, spatial coverage, and regional specificity that warrant clarification. The use of PSInSAR inherently constrains deformation retrieval in non-urban or vegetated terrain, where the density of coherent radar scatterers is low, and phase stability cannot be reliably maintained. This often results in spatial gaps in displacement measurements, especially outside built-up areas where permanent scatterers are limited [125]. Although this study focuses on urban ground settlement susceptibility, where PSInSAR performs robustly, future work will incorporate a combined PS-DS InSAR framework to increase measurement coverage in rural and vegetation-dominated zones [126]. Further, the model also inherits sensitivity to the accuracy and spatial resolution of the input datasets. Although a high-resolution DEM, soil-depth map, and a dense in situ V_s^{30} database were used to reduce uncertainty, errors in geotechnical (i.e., V_s^{30}), topographic, or seismological (i.e., use of a single NGA

model) layers may still propagate into the susceptibility estimates. Moreover, the building damage and sand blows/liquefaction/lateral spreading evidence used for validation were digitized from previously published maps (i.e., [15,21,23,58]); thus, positional uncertainties (georeferencing and digitization errors) in the source datasets may influence the final accuracy metrics. The research framework presented here is scalable to other seismically active and reclaimed coastal regions, where subsidence is influenced by anthropogenic loading and sediment consolidation. While the overall modeling framework is conceptually transferable to other regions, the trained models are region-specific. Application to areas with different soil compositions, seismic regimes, deformation processes, or land use histories would require retraining or recalibration using local geotechnical, seismological, topographical, and PSInSAR-based VLM datasets to ensure reliable performance.

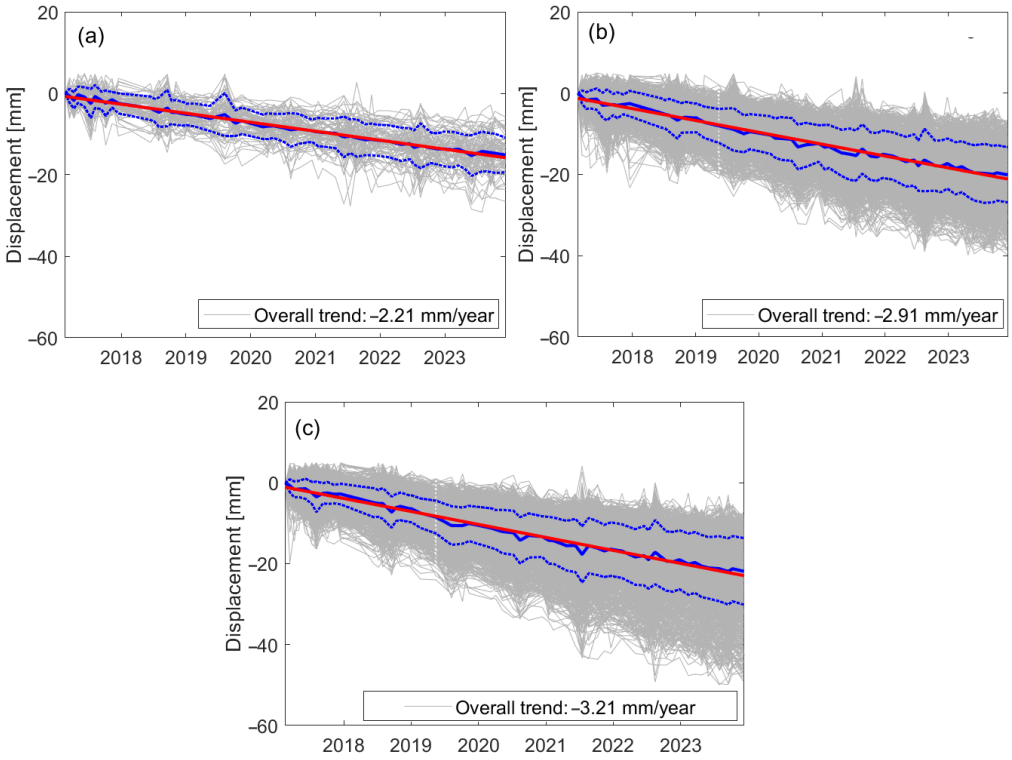

Figure 13. The generic settlement trends (red line) for (**a**) moderate-, (**b**) high-, and (**c**) very-high-GSS zones. The gray lines represent individual PS displacement histories, the red line denotes the overall settlement trend, and the blue line indicates (mean ± one standard deviation) the smoothed displacement variation through time.

The anticipated GSS zonation map provides a practical basis for prioritizing interventions in "high" and "very high" zones, where structures are most vulnerable to settlement during seismic loading. These areas can be targeted for measures such as seismic retrofitting, foundation stiffening, or the application of ground-improvement techniques, including deep mixing, compaction grouting, vibro-compaction, prefabricated vertical drains, and other densification methods. The GSS map may also support land use planning by identifying zones where new development should be avoided or where construction should proceed only with detailed geotechnical investigations and deformation-resistant design. Thus, the GSS zonation map serves as a decision-support tool for both immediate risk mitigation and long-term urban planning in seismically active, reclaimed, and alluvial environments. In future work, we also plan to incorporate a hyperbolic settlement model [25,127] to determine the nonlinear progression of consolidation and estimate long-term vertical displacements across different GSS zones. This will enhance the predic-

tive capability of the framework and support more detailed engineering assessments of settlement progression.

This study demonstrates that combining PSInSAR, ensemble machine learning, and multi-source geospatial datasets offers a comprehensive framework for assessing ground settlement susceptibility. The proposed approach offers critical insights into hazard mitigation and infrastructure resilience in seismically active, rapidly urbanizing regions, such as Pohang, by explicitly linking deformation to its geotechnical and seismic drivers. Furthermore, the findings highlight the broader seismic risk concerns in southeastern South Korea, where the combination of moderate seismicity, shallow earthquake sources, and vulnerable sedimentary basins creates a disproportionate potential for damage.

6. Conclusions

This study presented an integrated framework for assessing GSS in the Pohang region of South Korea by combining PSInSAR-derived deformation data with seismic, geotechnical, and topographic parameters using an ensemble of machine learning algorithms. The analysis of 56 Sentinel-1 images from 2017 to 2023 revealed ongoing subsidence concentrated in Quaternary alluvium, basin fill, reclaimed coastal plains, and riverine alluvial deposits, which are inherently prone to post-seismic consolidation and secondary settlement. Consequently, we utilize PSInSAR-derived VLM as a proxy for ML-based GSS modeling to enhance disaster preparedness and mitigate cascading risks in urban environments constructed on geologically fragile foundations. We considered eight geotechnical, topographical, and seismological attributes, including soil depth, seismic site class, landform class, slope, site period, general amplification factor, K_g, and PGA, as variables that influence settlement. Among the tested algorithms, RF and XGBoost demonstrated a superior predictive performance compared to the single-tree model (DT), underscoring the value of ensemble learning in capturing the nonlinear interactions that govern ground deformation. The model's generalization, along with the strong agreement between predicted and observed damage, supports the utility of RF-based susceptibility mapping for hazard assessment and risk mitigation in the study area. Integrating the optimal RF-based susceptibility map with building footprint revealed that nearly 65% of regional structures fall within high- or very-high-susceptibility zones, particularly in reclaimed port facilities, industrial areas, and dense residential clusters along the Hyeongsan River. These findings highlight the spatial convergence of geotechnical weakness and urban exposure, emphasizing the compounded vulnerability of critical assets to future seismic or settlement-induced damage.

While the present framework provides a robust regional assessment, further detailed geotechnical investigations are recommended to characterize the nonlinear soil behavior within high-risk zones. The outcomes of this study offer crucial insights for urban infrastructure management and policy development in seismically active sedimentary basins. These findings also underscore the urgent need to incorporate settlement susceptibility into national building codes, land use zoning, infrastructure design, and urban development planning to enhance resilience against multi-hazard risks.

Author Contributions: Conceptualization, W.J., M.-S.S., S.-G.Y. and M.D.A.; Methodology, W.J., M.-S.S. and M.D.A.; Software, M.-S.S. and M.D.A.; Validation, W.J., S.-G.Y. and M.D.A.; Formal analysis, M.-S.S. and M.D.A.; Investigation, M.-S.S., S.-G.Y. and M.D.A.; Resources, W.J., M.-S.S. and M.D.A.; Data curation, M.-S.S., S.-G.Y. and M.D.A.; Writing—original draft, W.J., M.-S.S., S.-G.Y. and M.D.A.; Writing—review & editing, W.J., M.-S.S., S.-G.Y. and M.D.A.; Visualization, S.-G.Y. and M.D.A.; Supervision, S.-G.Y.; Project administration, S.-G.Y.; Funding acquisition, S.-G.Y. All authors have read and agreed to the published version of the manuscript.

Funding: This work was supported by the National Research Foundation of Korea (NRF) grant funded by the Korea government (2021R1C1C2003316). This research was supported by the Regional

Innovation System & Education (RISE) program through the Gangwon RISE Center, funded by the Ministry of Education (MOE) and the Gangwon State (G.S.), Republic of Korea (2025-RISE-10-004).

Data Availability Statement: The original contributions presented in this study are included in the article. Further inquiries can be directed to the corresponding authors.

Acknowledgments: The authors would like to thank the SARPROZ team (https://www.sarproz.com/) for granting an evaluation license of the MT-InSAR processing program upon request. The authors also gratefully acknowledge the three anonymous reviewers and the Editors for their insightful comments and constructive suggestions, which have profoundly enhanced the scientific rigor, depth, and overall quality of the manuscript.

Conflicts of Interest: The authors declare no conflict of interest.

List of Abbreviations

A_F	General Amplification Factor
APS	Atmospheric Phase Screen
ASI	Amplitude Stability Index
DEM	Digital Elevation Model
DT	Decision Tree
ESA	European Space Agency
GIS	Geographic Information System
GMPE	Ground Motion Prediction Equation
GNSS	Global Navigation Satellite System
GPS	Global Positioning System
GSS	Ground Settlement Susceptibility
GSSM	Ground Settlement Susceptibility Zonation Map
IDW	Inverse Distance Weighted
IW	Interferometric Wide
K_g	Seismic Vulnerability Index
KRDA	Korea Rural Development Administration
LOS	Line of Sight
LPI	Liquefaction Potential Index
MAE	Mean Absolute Error
ML	Machine Learning
MSE	Mean Squared Error
NEHRP	National Earthquake Hazards Reduction Program
NGA	Next Generation Ground Motion Prediction Equation
NGII	National Geographic Information Institute
NSDI	Korea National Spatial Data Infrastructure
PGA	Peak Ground Acceleration
PS	Persistent Scatterers
PSInSAR	Persistent Scatterer Interferometric Synthetic Aperture Radar
RF	Random Forest
RMSE	Root Mean Squared Error
AUC–ROC	Receiver Operating Characteristic Curve
SAR	Synthetic Aperture Radar
SBAS	Small Baseline Subset
SLC	Single Look Complex
SPT	Standard Penetration Testing
TOPS	Terrain Observation with Progressive Scans
T_s	Site Period
VLM	Vertical Land Motion
$V_s{}^{30}$	Effective Shear-Wave Velocity
XGBoost	eXtreme Gradient Boosting

References

1. Dhahir, M.K.; Nadir, W.; Rasool, M.H. Influence of Soil Liquefaction on the Structural Performance of Bridges During Earthquakes: Showa Bridge as A Case Study. *Int. J. Eng. Technol.* **2018**, *7*, 146–152. [CrossRef]
2. Jeong, W.; Song, M.S.; Adhikari, M.D.; Yum, S.G. Monitoring the Integrity and Vulnerability of Linear Urban Infrastructure in a Reclaimed Coastal City Using SAR Interferometry. *Buildings* **2025**, *15*, 3865. [CrossRef]
3. Chaussard, E.; Amelung, F.; Abidin, H.; Hong, S.H. Sinking cities in Indonesia: ALOS PALSAR detects rapid subsidence due to groundwater and gas extraction. *Remote Sens. Environ.* **2013**, *128*, 150–161. [CrossRef]
4. Wu, P.C.; Wei, M.; D'Hondt, S. Subsidence in coastal cities throughout the world observed by InSAR. *Geophys. Res. Lett.* **2022**, *49*, e2022GL098477. [CrossRef]
5. Tay, C.; Lindsey, E.O.; Chin, S.T.; McCaughey, J.W.; Bekaert, D.; Nguyen, M.; Hua, H.; Manipon, G.; Karim, M.; Horton, B.P.; et al. Sea-level rise from land subsidence in major coastal cities. *Nat. Sustain.* **2022**, *5*, 1049–1057. [CrossRef]
6. Cabral-Cano, E.; Dixon, T.H.; Miralles-Wilhelm, F.; Díaz-Molina, O.; Sánchez-Zamora, O.; Carande, R.E. Space geodetic imaging of rapid ground subsidence in Mexico City. *Geol. Soc. Am. Bull.* **2008**, *120*, 1556–1566. [CrossRef]
7. Li, D.; Li, B.; Zhang, Y.; Fan, C.; Xu, H.; Hou, X. Spatial and temporal characteristics analysis for land subsidence in Shanghai coastal reclamation area using PS-InSAR method. *Front. Mar. Sci.* **2022**, *9*, 1000523. [CrossRef]
8. Seed, H.B.; Idriss, I.M. Analysis of soil liquefaction: Niigata earthquake. *J. Soil Mech. Found. Div.* **1967**, *93*, 83–108. [CrossRef]
9. Abdel-Haq, A.; Hryciw, R.D. Ground settlement in Simi Valley following the Northridge earthquake. *J. Geotech. Geoenvironmental Eng.* **1998**, *124*, 80–89. [CrossRef]
10. D'Ayala, D.; Free, M.; Bilham, R.; Doyle, P.; Evans, R.; Greening, P.; May, R.; Stewart, A.; Teymur, B.; Vince, D. *The Kocaeli, Turkey Earthquake of 17 August 1999*; Institution of Structural Engineers: London, UK, 2003.
11. Karanth, R.V.; Sohoni, P.S.; Mathew, G.; Khadkikar, A.S. Geological observations of the 26 January 2001 Bhuj earthquake. *J. Geol. Soc. India* **2001**, *58*, 193–202. [CrossRef]
12. Cubrinovski, M.; Bradley, B.; Wotherspoon, L.; Green, R.; Bray, J.; Wood, C.; Pender, M.; Allen, J.; Bradshaw, A.; Rix, G.; et al. Geotechnical aspects of the 22 February 2011 Christchurch earthquake. *Bull. New Zealand Soc. Earthq. Eng.* **2011**, *44*, 205–226. [CrossRef]
13. Tokimatsu, K.; Tamura, S.; Suzuki, H.; Katsumata, K. Building damage associated with geotechnical problems in the 2011 Tohoku Pacific Earthquake. *Soils Found.* **2012**, *52*, 956–974. [CrossRef]
14. Kim, H.S.; Sun, C.G.; Cho, H.I. Geospatial assessment of the post-earthquake hazard of the 2017 Pohang earthquake considering seismic site effects. *ISPRS Int. J. Geo-Inf.* **2018**, *7*, 375. [CrossRef]
15. Gihm, Y.S.; Kim, S.W.; Ko, K.; Choi, J.-H.; Bae, H.; Hong, P.S.; Lee, Y.; Lee, H.; Jin, K.; Choi, S.-J.; et al. Paleoseismological implications of liquefaction-induced structures caused by the 2017 Pohang Earthquake. *Geosci. J.* **2018**, *22*, 871–880. [CrossRef]
16. Naik, S.P.; Gwon, O.; Park, K.; Kim, Y.S. Land damage mapping and liquefaction potential analysis of soils from the epicentral region of 2017 Pohang Mw 5.4 earthquake, South Korea. *Sustainability* **2020**, *12*, 1234. [CrossRef]
17. Park, S.S.; Doan, N.P.; Nong, Z. Numerical prediction of settlement due to the Pohang earthquake. *Earthq. Spectra* **2021**, *37*, 652–685. [CrossRef]
18. Seo, H.; Kim, H.S.; Baise, L.G.; Kim, B. Geospatial liquefaction probability models based on sand boils occurred during the 2017 M5. 5 Pohang, South Korea, earthquake. *Eng. Geol.* **2024**, *329*, 107407. [CrossRef]
19. Naik, S.P.; Kim, Y.S.; Kim, T.; Su-Ho, J. Geological and structural control on localized ground effects within the Heunghae Basin during the Pohang Earthquake (M_W 5.4, 15th November 2017), South Korea. *Geosciences* **2019**, *9*, 173. [CrossRef]
20. Choi, J.H.; Ko, K.; Gihm, Y.S.; Cho, C.S.; Lee, H.; Song, S.G.; Bang, E.S.; Lee, H.J.; Bae, H.K.; Kim, S.W.; et al. Surface deformations and rupture processes associated with the 2017 Mw 5.4 Pohang, Korea, earthquake. *Bull. Seismol. Soc. Am.* **2019**, *109*, 756–769. [CrossRef]
21. Kim, B.; Ji, Y.; Kim, M.; Lee, Y.-J.; Kang, H.; Yun, N.-R.; Kim, H.; Lee, J. Building damage caused by the 2017 M5.4 Pohang, South Korea, earthquake, and effects of ground conditions. *J. Earthq. Eng.* **2022**, *26*, 3054–3072. [CrossRef]
22. Kim, H.S.; Kim, M.; Baise, L.G.; Kim, B. Local and regional evaluation of liquefaction potential index and liquefaction severity number for liquefaction-induced sand boils in Pohang, South Korea. *Soil Dyn. Earthq. Eng.* **2021**, *141*, 106459. [CrossRef]
23. Kang, S.; Kim, B.; Bae, S.; Lee, H.; Kim, M. Earthquake-induced ground deformations in the low-seismicity region: A case of the 2017 M5. 4 Pohang, South Korea, earthquake. *Earthq. Spectra* **2019**, *35*, 1235–1260. [CrossRef]
24. Nur, A.S.; Achmad, A.R.; Lee, C.W. Land subsidence measurement in reclaimed coastal land: Noksan using C-band sentinel-1 radar interferometry. *J. Coast. Res.* **2020**, *102*, 218–223. [CrossRef]
25. Park, S.W.; Hong, S.H. Nonlinear modeling of subsidence from a decade of InSAR time series. *Geophys. Res. Lett.* **2021**, *48*, e2020GL090970. [CrossRef]
26. Park, K.; Kim, Y.J.; Chen, J.; Nam, B.H. InSAR-based investigation of ground subsidence due to excavation: A case study of Incheon City, South Korea. *Int. J. Geo-Eng.* **2024**, *15*, 26. [CrossRef]

27. Sengupta, D.; Chen, R.; Meadows, M.E.; Banerjee, A. Gaining or losing ground? Tracking Asia's hunger for 'new'coastal land in the era of sea level rise. *Sci. Total Environ.* **2020**, *732*, 139290. [CrossRef]
28. Oh, D.W.; Kong, S.M.; Lee, D.Y.; Yoo, Y.S.; Lee, Y.J. Effects of Reinforced Pseudo-Plastic Backfill on the Behavior of Ground around Cavity Developed due to Sewer Leakage. *J. Korean Geoenvironmental Soc.* **2015**, *16*, 13–22. [CrossRef]
29. Lee, K.; Nam, J.; Park, J.; Hong, G. Numerical Analysis of Factors Influencing the Ground Surface Settlement above a Cavity. *Materials* **2022**, *15*, 8301. [CrossRef] [PubMed]
30. Jeon, S.S.; Park, Y.K.; Eum, K.Y. Stability assessment of roadbed affected by ground subsidence adjacent to urban railways. *Nat. Hazards Earth Syst. Sci.* **2018**, *18*, 2261–2271. [CrossRef]
31. Ohenhen, L.O.; Zhai, G.; Lucy, J.; Werth, S.; Carlson, G.; Khorrami, M.; Onyike, F.; Sadhasivam, N.; Tiwari, A.; Ghobadi-Far, K.; et al. Land subsidence risk to infrastructure in US metropolises. *Nat. Cities* **2025**, *2*, 543–554. [CrossRef]
32. Herrera-García, G.; Ezquerro, P.; Tomás, R.; Béjar-Pizarro, M.; López-Vinielles, J.; Rossi, M.; Mateos, R.M.; Carreón-Freyre, D.; Lambert, J.; Teatini, P.; et al. Mapping the global threat of land subsidence. *Science* **2021**, *371*, 34–36. [CrossRef] [PubMed]
33. Shirzaei, M.; Freymueller, J.; Törnqvist, T.E.; Galloway, D.L.; Dura, T.; Minderhoud, P.S. Measuring, modelling and projecting coastal land subsidence. *Nat. Rev. Earth Environ.* **2021**, *2*, 40–58. [CrossRef]
34. Yang, X.; Wu, H.; Zhou, S.; Guo, D.; Chen, R. Land subsidence in coastal reclamation with impact on metro operation under rapid urbanization: A case study of Shenzhen. *Sci. Total Environ.* **2025**, *970*, 179020. [CrossRef]
35. Zanjani, F.A.; Amelung, F.; Piter, A.; Sobhan, K.; Tavakkoliestahbanati, A.; Eberli, G.P.; Haghighi, M.H.; Motagh, M.; Milillo, P.; Mirzaee, S.; et al. Insar observations of construction-induced coastal subsidence on Miami's barrier islands, Florida. *Earth Space Sci.* **2024**, *11*, e2024EA003852.
36. Sun, X.; Chen, X.; Yang, L.; Wang, W.; Zhou, X.; Wang, L.; Yao, Y. Using insar and polsar to assess ground displacement and building damage after a seismic event: Case study of the 2021 baicheng earthquake. *Remote Sens.* **2022**, *14*, 3009. [CrossRef]
37. Suresh, D.; Yarrakula, K. InSAR based deformation mapping of earthquake using Sentinel 1A imagery. *Geocarto Int.* **2020**, *35*, 559–568. [CrossRef]
38. Yun, H.W.; Kim, J.R.; Yoon, H.; Choi, Y.; Yu, J. Seismic surface deformation risks in industrial hubs: A case study from Ulsan, Korea, using DInSAR time series analysis. *Remote Sens.* **2019**, *11*, 1199. [CrossRef]
39. Palanisamy Vadivel, S.K.; Kim, D.J.; Jung, J.; Cho, Y.K.; Han, K.J.; Jeong, K.Y. Sinking tide gauge revealed by space-borne InSAR: Implications for sea level acceleration at Pohang, South Korea. *Remote Sens.* **2019**, *11*, 277. [CrossRef]
40. Ramirez, R.; Lee, S.R.; Kwon, T.H. Long-term remote monitoring of ground deformation using sentinel-1 interferometric synthetic aperture radar (InSAR): Applications and insights into geotechnical engineering practices. *Appl. Sci.* **2020**, *10*, 7447. [CrossRef]
41. Chai, L.; Xie, X.; Wang, C.; Tang, G.; Song, Z. Ground subsidence risk assessment method using PS-InSAR and LightGBM: A case study of Shanghai metro network. *Int. J. Digit. Earth* **2024**, *17*, 2297842. [CrossRef]
42. Chen, C.; Peng, M.; Motagh, M.; Guo, X.; Xing, M.; Quan, Y. Mapping susceptibility and risk of land subsidence by integrating InSAR and hybrid machine learning models: A case study in Xi'an, China. *IEEE J. Sel. Top. Appl. Earth Obs. Remote Sens.* **2025**, *18*, 3625–3639. [CrossRef]
43. Fadhillah, M.F.; Achmad, A.R.; Lee, C.W. Integration of InSAR time-series data and GIS to assess land subsidence along subway lines in the Seoul metropolitan area, South Korea. *Remote Sens.* **2020**, *12*, 3505. [CrossRef]
44. Hussain, S.; Pan, B.; Afzal, Z.; Sajjad, M.M.; Kakar, N.; Ahmed, N.; Hussain, W.; Ali, M. SBAS-InSAR Analysis of tectonic derived ground deformation and subsidence susceptibility mapping via machine learning in Quetta City, Pakistan. *Int. J. Digit. Earth* **2025**, *18*, 2441926. [CrossRef]
45. Lu, C.; Xu, H.; Yao, Q.; Liu, Q.; Bricker, J.D.; Jonkman, S.N.; Yin, J.; Wang, J. Tracking 30-year evolution of subsidence in Shanghai utilizing multi-sensor InSAR and random forest modelling. *Int. J. Appl. Earth Obs. Geoinf.* **2025**, *140*, 104606. [CrossRef]
46. Sharma, G.; Singh, M.S.; Nayak, K.; Dutta, P.P.; Sarma, K.K.; Aggarwal, S.P. Earthquake Damage Susceptibility Analysis in Barapani Shear Zone Using InSAR, Geological, and Geophysical Data. *Geosciences* **2025**, *15*, 45. [CrossRef]
47. Tian, F.; Zhang, W.; Zhu, H.H.; Wang, C.; Chang, F.N.; Li, H.Z.; Tan, D.Y. Multi-temporal InSAR-based landslide dynamic susceptibility mapping of Fengjie County, Three Gorges Reservoir Area, China. *J. Rock Mech. Geotech. Eng.* **2025**. [CrossRef]
48. Yaragunda, V.R.; Vaka, D.S.; Oikonomou, E. Land Subsidence Susceptibility Modelling in Attica, Greece: A Machine Learning Approach Using InSAR and Geospatial Data. *Earth* **2025**, *6*, 61. [CrossRef]
49. Zeng, T.; Wu, L.; Hayakawa, Y.S.; Yin, K.; Gui, L.; Jin, B.; Guo, Z.; Peduto, D. Advanced integration of ensemble learning and MT-InSAR for enhanced slow-moving landslide susceptibility zoning. *Eng. Geol.* **2024**, *331*, 107436. [CrossRef]
50. Zhao, F.; Miao, F.; Wu, Y.; Xiong, Y.; Gong, S.; Sun, D. Land subsidence susceptibility mapping in urban settlements using time-series PS-InSAR and random forest model. *Gondwana Res.* **2024**, *125*, 406–424. [CrossRef]
51. Jin, B.; Zeng, T.; Wang, T.; Zhang, Z.; Gui, L.; Yin, K.; Zhao, B. Advanced risk assessment framework for land subsidence impacts on transmission towers in salt lake region. *Environ. Model. Softw.* **2024**, *177*, 106058. [CrossRef]
52. Kim, H.S. Geospatial data-driven assessment of earthquake-induced liquefaction impact mapping using classifier and cluster ensembles. *Appl. Soft Comput.* **2023**, *140*, 110266. [CrossRef]

53. Zhao, F.; Miao, F.; Wu, Y.; Ke, C.; Gong, S.; Ding, Y. Refined landslide susceptibility mapping in township area using ensemble machine learning method under dataset replenishment strategy. *Gondwana Res.* **2024**, *131*, 20–37. [CrossRef]
54. Zhang, Y.; Jiao, Y.Y.; He, L.L.; Tan, F.; Zhu, H.M.; Wei, H.L.; Zhang, Q.B. Susceptibility mapping and risk assessment of urban sinkholes based on grey system theory. *Tunn. Undergr. Space Technol.* **2024**, *152*, 105893. [CrossRef]
55. Park, S.; Hong, T.K.; Rah, G. Seismic hazard assessment for the Korean Peninsula. *Bull. Seismol. Soc. Am.* **2021**, *111*, 2696–2719. [CrossRef]
56. Hong, T.K.; Lee, J.; Park, S.; Kim, W. Major influencing factors for the nucleation of the 15 November 2017 Mw 5.5 Pohang earthquake. *Phys. Earth Planet. Inter.* **2022**, *323*, 106833. [CrossRef]
57. Lee, K.; Yang, W.S. Historical seismicity of Korea. *Bull. Seismol. Soc. Am.* **2006**, *96*, 846–855. [CrossRef]
58. Seon, C.G.; Kim, H.S.; Cho, H.I. Investigation and analysis of Pohang Earthquake in Relation to Geotechnical Earthquake Engineering. In Proceedings of the Symposium on Characteristics of Pohang Earthquake and Countermeasures for Geotechnical Structure, Seoul, Republic of Korea, 7 February 2018. Available online: https://www.ksce.or.kr/not/Default.asp?page=1&bidx=48219&sfield=&gtxt=&gbn=13&bcat=&ctop=&htop=&ptop=&idx=&bgbn=R (accessed on 20 November 2025).
59. Chough, S.K.; Kwon, S.T.; Ree, J.H.; Choi, D.K. Tectonic and sedimentary evolution of the Korean peninsula: A review and new view. *Earth-Sci. Rev.* **2000**, *52*, 175–235. [CrossRef]
60. Choi, J.H.; Kim, Y.S.; Choi, S.J. Identification of a suspected Quaternary fault in eastern Korea: Proposal for a paleoseismic research procedure for the mapping of active faults in Korea. *J. Asian Earth Sci.* **2015**, *113*, 897–908. [CrossRef]
61. Jang, C.J.; Shin, J.S.; Heo, T.Y.; Lee, J.L. Behavioral characteristics of the Yangsan fault based on geometric analysis. In Proceedings of the 1999 Autumn Meeting of the Korean Nuclear Society, Seoul, Republic of Korea, 29–30 October 1999.
62. Han, J.; Nur, A.S.; Syifa, M.; Ha, M.; Lee, C.W.; Lee, K.Y. Improvement of Earthquake Risk Awareness and Seismic Literacy of Korean Citizens through Earthquake Vulnerability Map from the 2017 Pohang Earthquake, South Korea. *Remote Sens.* **2021**, *13*, 1365. [CrossRef]
63. Hanssen, R.F. *Radar Interferometry: Data Interpretation and Error Analysis*; Springer Science & Business Media: Berlin/Heidelberg, Germany, 2001; Volume 2.
64. He, H.; Zhou, L.; Lee, H. Ground displacement variation around power line corridors on the loess plateau estimated by persistent scatterer interferometry. *IEEE Access* **2021**, *9*, 87908–87917. [CrossRef]
65. Kirui, P.; Oiro, S.; Waithaka, H.; Odera, P.; Riedel, B.; Gerke, M. Detection, characterization, and analysis of land subsidence in Nairobi using InSAR. *Nat. Hazards* **2022**, *113*, 213–236. [CrossRef]
66. Qin, Y.; Perissin, D.; Bai, J. Investigations on the coregistration of Sentinel-1 TOPS with the conventional cross-correlation technique. *Remote Sens.* **2018**, *10*, 1405. [CrossRef]
67. Kim, B.; Hong, T.K. A national $V_s{}^{30}$ model for South Korea to combine nationwide dense borehole measurements with ambient seismic noise analysis. *Earth Space Sci.* **2022**, *9*, e2021EA002066. [CrossRef]
68. Allen, T.I.; Wald, D.J. On the use of high-resolution topographic data as a proxy for seismic site conditions ($V_S{}^{30}$). *Bull. Seismol. Soc. Am.* **2009**, *99*, 935–943. [CrossRef]
69. Ahmad, R.A. Seismic microzonation map of Syria using topographic slope and characteristics of surface soil. *Nat. Hazards* **2016**, *80*, 1323–1347. [CrossRef]
70. Nakamura, Y. Seismic vulnerability indices for ground and structures using microtremor. In Proceedings of the World Congress on Railway Research, Florence, Italy, 16–19 November 1997.
71. Sil, A.; Sitharam, T.G. Detection of Local Site Conditions in Tripura and Mizoram Using the Topographic Gradient Extracted from Remote Sensing Data and GIS Techniques. *Nat. Hazards Rev.* **2017**, *18*, 04016009. [CrossRef]
72. Emolo, A.; Sharma, N.; Festa, G.; Zollo, A.; Convertito, V.; Park, J.; Chi, H.; Lim, I. Ground-motion prediction equations for South Korea Peninsula. *Bull. Seismol. Soc. Am.* **2015**, *105*, 2625–2640. [CrossRef]
73. Ferretti, A.; Prati, C.; Rocca, F. Permanent scatterers in SAR interferometry. *IEEE Trans. Geosci. Remote Sens.* **2001**, *39*, 8–20. [CrossRef]
74. Perissin, D.; Wang, Z.; Wang, T. The SARPROZ InSAR tool for urban subsidence/man-made structure stability monitoring in China. In Proceedings of the 34th International Symposium on Remote Sensing of Environment, ISRSE, Sidney, Australia, 10–15 April 2011; p. 1015.
75. Xu, H.; Chen, F.; Zhou, W. A comparative case study of MTInSAR approaches for deformation monitoring of the cultural landscape of the Shanhaiguan section of the Great Wall. *Herit. Sci.* **2021**, *9*, 1–5. [CrossRef]
76. Yang, F.; Zhi, M.; An, Y. Revealing large-scale surface subsidence in Jincheng City's mining clusters using MT-InSAR and VMD-SSA-LSTM time series prediction model. *Sci. Rep.* **2025**, *15*, 5726. [CrossRef] [PubMed]
77. Ramirez, R.A.; Lee, G.J.; Choi, S.K.; Kwon, T.H.; Kim, Y.C.; Ryu, H.H.; Kim, S.; Bae, B.; Hyun, C. Monitoring of construction-induced urban ground deformations using Sentinel-1 PS-InSAR: The case study of tunneling in Dangjin, Korea. *Int. J. Appl. Earth Obs. Geoinf.* **2022**, *108*, 102721. [CrossRef]

78. Hussain, S.; Pan, B.; Afzal, Z.; Ali, M.; Zhang, X.; Shi, X.; Ali, M. Landslide detection and inventory updating using the time-series InSAR approach along the Karakoram Highway, Northern Pakistan. *Sci. Rep.* **2023**, *13*, 7485. [CrossRef]
79. Shen, P.; Wang, C.; Hu, C.; Luo, X. PS-ESD: Persistent scatterer-based enhanced spectral diversity approach for time-series Sentinel-1 TOPS data co-registration. *IEEE Geosci. Remote Sens. Lett.* **2022**, *19*, 1–5. [CrossRef]
80. Khoshlahjeh Azar, M.; Hamedpour, A.; Maghsoudi, Y.; Perissin, D. Analysis of the deformation behavior and sinkhole risk in Kerdabad, Iran using the PS-InSAR method. *Remote Sens.* **2021**, *13*, 2696. [CrossRef]
81. Adhikari, M.D.; Park, S.; Yum, S.G. Coastal vulnerability to extreme weather events: An integrated analysis of erosion, sediment movement, and land subsidence based on multi-temporal optical and SAR satellite data. *J. Environ. Manag.* **2025**, *374*, 124025. [CrossRef]
82. Qiao, X.; Chu, T.; Tissot, P.; Holland, S. Sentinel-1 InSAR-derived land subsidence assessment along the Texas Gulf Coast. *Int. J. Appl. Earth Obs. Geoinf.* **2023**, *125*, 103544. [CrossRef]
83. Khorrami, M.; Abrishami, S.; Maghsoudi, Y.; Alizadeh, B.; Perissin, D. Extreme subsidence in a populated city (Mashhad) detected by PSInSAR considering groundwater withdrawal and geotechnical properties. *Sci. Rep.* **2020**, *10*, 11357. [CrossRef]
84. Fárová, K.; Jelének, J.; Kopačková-Strnadová, V.; Kycl, P. Comparing DInSAR and PSI techniques employed to Sentinel-1 data to monitor highway stability: A case study of a massive Dobkovičky landslide, Czech Republic. *Remote Sens.* **2019**, *11*, 2670. [CrossRef]
85. Hussain, M.A.; Chen, Z.; Shoaib, M.; Shah, S.U.; Khan, J.; Ying, Z. Sentinel-1A for monitoring land subsidence of coastal city of Pakistan using Persistent Scatterers In-SAR technique. *Sci. Rep.* **2022**, *12*, 5294. [CrossRef]
86. Jung, J.; Kim, D.J.; Palanisamy Vadivel, S.K.; Yun, S.H. Long-term deflection monitoring for bridges using X and C-band time-series SAR interferometry. *Remote Sens.* **2019**, *11*, 1258. [CrossRef]
87. Wang, K.; Chen, J.; Valseth, E.; Wells, G.; Bettadpur, S.; Jones, C.E.; Dawson, C. Subtle land subsidence elevates future storm surge risks along the gulf coast of the United States. *J. Geophys. Res. Earth Surf.* **2024**, *129*, e2024JF007858. [CrossRef]
88. Adhikari, M.D.; Song, M.S.; Yum, S.G. The impact of climate change and localized land subsidence along the Korean Peninsula Coastline: An Overview of future coastal inundation and vulnerability. *Int. J. Appl. Earth Obs. Geoinf.* **2025**, *144*, 104894. [CrossRef]
89. Buzzanga, B.; Bekaert, D.P.; Hamlington, B.D.; Kopp, R.E.; Govorcin, M.; Miller, K.G. Localized uplift, widespread subsidence, and implications for sea level rise in the New York City metropolitan area. *Sci. Adv.* **2023**, *9*, eadi8259. [CrossRef] [PubMed]
90. Kang, S.Y.; Kim, K.H.; Choi, M.; Park, S.C. Ground vulnerability derived from the horizontal-to-vertical spectral ratio: Comparison with the damage distribution caused by the 2017 ML 5.4 Pohang earthquake, Korea. *Near Surf. Geophys.* **2021**, *19*, 155–167. [CrossRef]
91. Wald, D.J.; Allen, T.I. Topographic slope as a proxy for seismic site conditions and amplification. *Bull. Seismol. Soc. Am.* **2007**, *97*, 1379–1395. [CrossRef]
92. Shafique, M.; Hussain, M.L.; Khan, M.A.; van der Meijde, M.; Khan, S. Geology as a proxy for Vs30-based seismic site characterization, a case study of northern Pakistan. *Arab. J. Geosci.* **2018**, *11*, 298. [CrossRef]
93. Gilder, C.E.; De Risi, R.; De Luca, F.; Mohan Pokhrel, R.; Vardanega, P.J. Geostatistical framework for estimation of $V_S{}^{30}$ in data-scarce regions. *Bull. Seismol. Soc. Am.* **2022**, *112*, 2981–3000. [CrossRef]
94. Sahin, G.; Okalp, K.; Kockar, M.K.; Yilmaz, M.T.; Jalehforouzan, A.; Temiz, F.A.; Askan, A.; Akgun, H.; Erberik, M.A. Development of a GIS-Based Predicted-VS 30 Map of Türkiye Using Geological and Topographical Parameters: Case Study for the Region Affected by the 6 February 2023 Kahramanmaraş Earthquakes. *Seismol. Res. Lett.* **2024**, *95*, 2044–2057. [CrossRef]
95. Thakur, H.; Anbazhagan, P. Geology, geomorphology and $V_s{}^{30}$-based site classification of the Himalayan region using a stacked model. *Eng. Geol.* **2025**, *355*, 108229. [CrossRef]
96. Borcherdt, R.D. Estimates of site-dependent response spectra for design (methodology and justification). *Earthq. Spectra* **1994**, *10*, 617. [CrossRef]
97. IBC 2006. *International Building Code*; International Code Council, Inc.: Country Club Hills, IL, USA, 2006.
98. Brown, L.T.; Boore, D.M.; Stokoe, K.H. Comparison of shear-wave slowness profiles at 10 strong-motion sites from noninvasive SASW measurements and measurements made in boreholes. *Bull. Seismol. Soc. Am.* **2002**, *92*, 3116–3133. [CrossRef]
99. Shearer, P.M. *Introduction to Seismology*; Cambridge University Press: Cambridge, UK, 1999; p. 260.
100. Boore, D.M.; Joyner, W.B. Site amplifications for generic rock sites. *Bull. Seismol. Soc. Am.* **1997**, *87*, 327–341. [CrossRef]
101. Mase, L.Z.; Sugianto, N. Seismic hazard microzonation of Bengkulu City, Indonesia. *Geo-Environ. Disasters* **2021**, *8*, 5. [CrossRef]
102. Huang, H.C.; Tseng, Y.S. Characteristics of soil liquefaction using H/V of microtremors in Yuan-Lin area, Taiwan. *Terr. Atmos. Ocean. Sci.* **2002**, *13*, 325–338. [CrossRef]
103. Kang, S.Y.; Kim, K.H.; Kim, B. Assessment of seismic vulnerability using the horizontal-to-vertical spectral ratio (HVSR) method in Haenam, Korea. *Geosci. J.* **2020**, *25*, 71–81. [CrossRef]
104. Singh, A.P.; Shukla, A.; Kumar, M.R.; Thakkar, M.G. Characterizing Surface Geology, Liquefaction Potential, and Maximum Intensity in the Kachchh Seismic Zone, Western India, through Microtremor Analysis Characterizing Surface Geology, Liquefaction Potential, and Maximum Intensity in the Kachchh Seismic Zone. *Bull. Seismol. Soc. Am.* **2017**, *107*, 1277–1292. [CrossRef]

105. Choobbasti, A.; Naghizaderokni, M.; Naghizaderokni, M. Reliability analysis of soil liquefaction based on standard penetration: A case study in Babol city. In Proceedings of the 2015 International Conference on Sustainable Civil Engineering (ICSCE 2015), Chengdu, China, 19–20 September 2015.
106. Mantovani, J.; Enner. Unraveling the Ground Subsidence Disaster Caused by Rock Salt Mining in Maceió (Northeast Brazil) from 2020 Until Rupture Using Sentinel-1 Data. 2024. Available online: https://www.researchsquare.com/article/rs-3826573/v1 (accessed on 25 November 2025).
107. Youd, T.L.; Perkins, D.M. Mapping liquefaction-induced ground failure potential. *J. Geotech. Eng. Div.* **1978**, *104*, 433–446. [CrossRef]
108. Ganapathy, G.P.; Rajawat, A.S. Evaluation of liquefaction potential hazard of Chennai city, India: Using geological and geomorphological characteristics. *Nat. Hazards* **2012**, *64*, 1717–1729. [CrossRef]
109. Ortiz-Hernández, E.; Chunga, K.; Toulkeridis, T.; Pastor, J.L. Soil liquefaction and other seismic-associated phenomena in the city of Chone during the 2016 Earthquake of Coastal Ecuador. *Appl. Sci.* **2022**, *12*, 7867. [CrossRef]
110. Qin, Y.; Cao, L.; Li, S.; Ye, F.; Boloorani, A.D.; Liang, Z.; Huang, J.; Liu, G. Multisource geoscience data-driven framework for subsidence risk assessment in urban area. *Int. J. Disaster Risk Reduct.* **2024**, *113*, 104901. [CrossRef]
111. Zhu, Y.; Chen, H.; Sun, D.; Zhu, X.; Ji, Q.; Wen, H.; Zhang, Q.; Wu, R. A heterogeneous ensemble landslide susceptibility assessment method based on InSAR and geographic similarity extended landslide inventory. *Gondwana Res.* **2025**, *144*, 181–196. [CrossRef]
112. Roy, M.H.; Larocque, D. Robustness of random forests for regression. *J. Nonparametric Stat.* **2012**, *24*, 993–1006. [CrossRef]
113. Yıldırım, H. The multicollinearity effect on the performance of machine learning algorithms: Case examples in healthcare modelling. *Acad. Platf. J. Eng. Smart Syst.* **2024**, *12*, 68–80. [CrossRef]
114. Chowdhury, S.; Lin, Y.; Liaw, B.; Kerby, L. Evaluation of tree based regression over multiple linear regression for non-normally distributed data in battery performance. In Proceedings of the 2022 International Conference on Intelligent Data Science Technologies and Applications (IDSTA), San Antonio, TX, USA, 5–7 September 2022; IEEE: New York, NY, USA; pp. 17–25.
115. Adhikari, M.D.; Yum, S.G.; Yune, C.Y. Geospatial-based risk analysis of solar plants located in the mountainous region of Gangwon Province, South Korea. *Renew. Energy* **2025**, *251*, 123408. [CrossRef]
116. Gelman, A.; Hill, J. *Data Analysis Using Regression and Multilevel/Hierarchical Models*; Cambridge University Press: New York, NY, USA, 2007; ISBN 0-521-86706-1.
117. Tuganishuri, J.; Yune, C.Y.; Kim, G.; Lee, S.W.; Adhikari, M.D.; Yum, S.G. Prediction of the volume of shallow landslides due to rainfall using data-driven models. *Nat. Hazards Earth Syst. Sci.* **2025**, *25*, 1481–1499. [CrossRef]
118. Breiman, L. Random forests. *Mach. Learn.* **2001**, *45*, 5–32. [CrossRef]
119. Chen, T.; He, T.; Benesty, M.; Khotilovich, V.; Tang, Y.; Cho, H.; Chen, K.; Mitchell, R.; Cano, I.; Zhou, T.; et al. xgboost: Extreme Gradient Boosting. *R Package Version 1.6.0.1*. 2022. Available online: https://CRAN.R-project.org/package=xgboost (accessed on 20 July 2025).
120. Arabameri, A.; Saha, S.; Roy, J.; Chen, W.; Blaschke, T.; Tien Bui, D. Landslide susceptibility evaluation and management using different machine learning methods in the Gallicash River Watershed, Iran. *Remote Sens.* **2020**, *12*, 475. [CrossRef]
121. Shahabi, H.; Hashim, M. Landslide susceptibility mapping using GIS-based statistical models and Remote sensing data in tropical environment. *Sci. Rep.* **2015**, *5*, 9899. [CrossRef]
122. Ayalew, L.; Yamagishi, H.; Marui, H.; Kanno, T. Landslides in Sado Island of Japan: Part II. GIS-based susceptibility mapping with comparisons of results from two methods and verifications. *Eng. Geol.* **2005**, *81*, 432–445. [CrossRef]
123. Chiaro, G.; Koseki, J. Liquefaction and Failure Mechanisms of Sandy Sloped Ground during Earthquakes: A Comparison between Laboratory and Field Observations. In Proceedings of the Australian Earthquake Engineering Society Conference 2012, Gold Coast, Australia, 7–9 December 2012.
124. Dashti, S.; Bray, J.D.; Pestana, J.M.; Riemer, M.; Wilson, D. Mechanisms of seismically induced settlement of buildings with shallow foundations on liquefiable soil. *J. Geotech. Geoenvironmental Eng.* **2010**, *136*, 151–164. [CrossRef]
125. ElGharbawi, T.; Tamura, M. Increasing spatial coverage in rough terrain and vegetated areas using InSAR optimized pixel selection: Application to Tohoku, Japan. *Geo-Spat. Inf. Sci.* **2022**, *25*, 295–311. [CrossRef]
126. Liu, Y.; Yang, H.; Wang, S.; Xu, L.; Peng, J. Monitoring and stability analysis of the deformation in the Woda landslide area in Tibet, China by the DS-InSAR method. *Remote Sens.* **2022**, *14*, 532. [CrossRef]
127. Tan, T.S.; Inoue, T.; Lee, S.L. Hyperbolic method for consolidation analysis. *J. Geotech. Eng.* **1991**, *117*, 1723–1737. [CrossRef]

Disclaimer/Publisher's Note: The statements, opinions and data contained in all publications are solely those of the individual author(s) and contributor(s) and not of MDPI and/or the editor(s). MDPI and/or the editor(s) disclaim responsibility for any injury to people or property resulting from any ideas, methods, instructions or products referred to in the content.